Alma Mater Studiorum – University of Bologna

SCHOOL OF SCIENCE
Department of Industrial Chemistry “Toso Montanari”

Second cycle degree in

Low Carbon Technologies and Sustainable Chemistry

Classe LM-75 - Scienza e Tecnologie per l’Ambiente e il Territorio

Redox-sensitive PMMA-core-shell nanoparticles as drug carriers for anti-cancer therapeutics

CANDIDATE

Andrey Sergeev Kurtev

SUPERVISOR

Chiar.ma Prof. Mariafrancesca Fochi

CO-SUPERVISOR

Dott. Greta Varchi

Academic Year 2020-2021

Table of Contents

List of abbreviations:

CPT – Camptothecin
DSDMA - Bis(2-methacryloyl) oxyethyl disulfide
DTT - Dithiothreitol
MAACl – Methacrolyl chloride
EPR – Enhanced permeability and retention
GSH – Gluthathione
NP – Nanoparticle
MAAnh – Methacrylic anhydride
NPs – Nanoparticles
TGA – Thermogravimetric analysis
PAX - Paclitaxel
DOX - Doxorubicin
PDT – Photodynamic therapy
MMA – Methyl methacrylate
PMMA – Polymethyl methacrylate
PS - Photosensitizer
ROS – Reactive oxygen species
TAR - 2-(dimethyl-octyl) ammonium ethyl methacrylate bromide

1 Introduction

1.1 The scope and severity of the cancer problem (globally).

Cancer has been given as a diagnosis to 19.3 million people in 2020 and has caused the death of 10 million. Those numbers are projected to increase to 28.4 and 16 million by the year 2040. Cancer has been the leading cause of death in most developed countries for decades and is gaining ground around the world. (Sung et al., 2021).

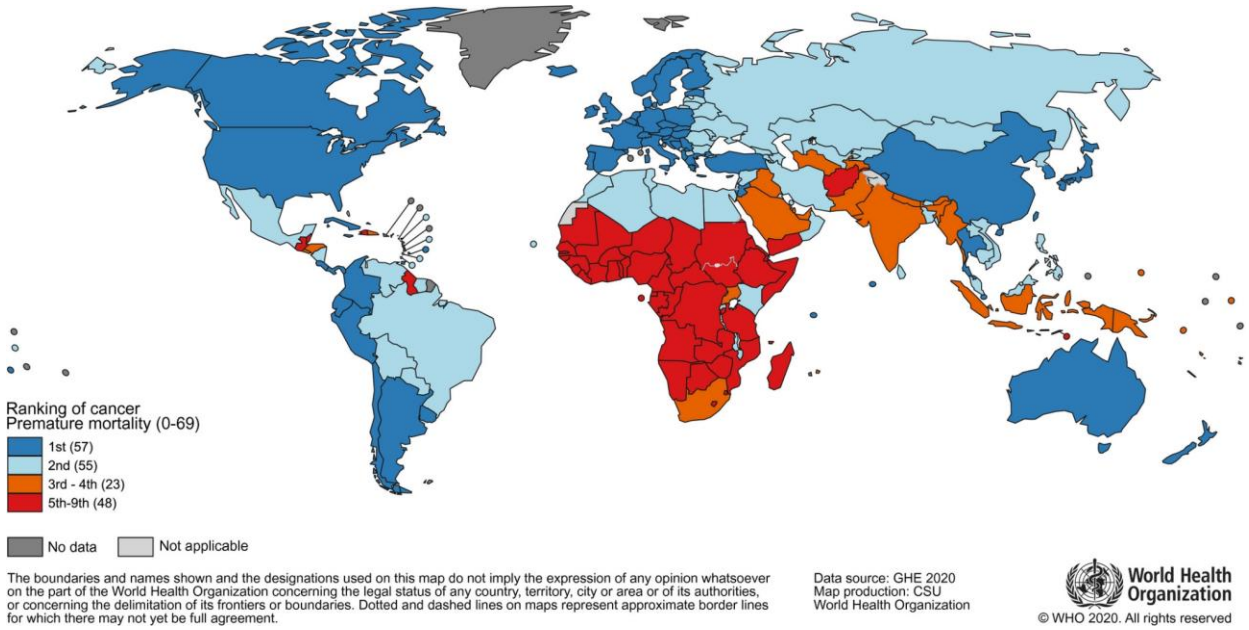

Figure 1: Ranking of cancer as a lead cause of premature mortality across the globe.
Note: Cancer ranks 1st in most developed countries and 2nd and 3rd in many developing countries. It has a lower ranking only in countries with considerable health and social issues
From Global Cancer Statistics 2020: GLOBOCAN by Sung et al. https://doi.org/10.3322/caac.21660

The disease is related, on average, to 15 years of life lost per victim. Furthermore, expenses related to diagnosis and treatment amount to billions, covered both by the patient and the health care systems. (Hofmarcher et al., 2020) Despite their dreadfulness, these statistics only outline the socio-economic effects of cancer, while hiding the devastating effect on the lives of individuals.

Combating the increase in cancer rate is not easy, nor straightforward as cancer is a complex, severe and persistent condition. Nevertheless, the problem can be approached through prevention, diagnosis and treatment. Reliable prevention, of course, is the most desirable approach as it avoids the problem altogether, however, it poses a global-scale life-long challenge. (Meyskens et al.,2015)

1.1.1 Risk factors and difficulty of prevention

Part of the challenge stems from the fact that carcinogenesis is a very complex and varied process. Some of the causes for the disease are still not fully understood, despite several decades of study. (Bizzarri et al., 2008) Nonetheless, many risk factors have been discovered and studied for the development of prevention strategies. Most prominently among them - extrinsic risk factors related to behaviors and lifestyles, involving smoking, alcohol use, lack of physical activity, unhealthy diet, infections, exposure to cancerogenic substances etc. (Stein & Colditz, 2004) Extrinsic factors can, in theory, be fully controlled. In reality, and on a global scale, this would take significant time and effort, as most of the factors are strongly incorporated into the modern way of life. Furthermore - large scale phenomena, such as air pollution (from forest fires, fossil fuel burning etc.), drinking water pollution (industrial chemicals, heavy metals etc.) and UV radiation are also recognized as extrinsic risk factors and are extremely difficult to control. (Boffetta & Nyberg, 2003; Armstrong & Kricker, 2001)

Moreover, non-preventable (intrinsic) risk factors - the random accumulation of genetic errors and semi-preventable risk factors such as biological aging, hormonal imbalances and inflammation, steadily contribute to cancer's incidence rate. With the increase in average age/lifespan of the population and the increased survivability of genetically burdened individuals due to the advances of modern medicine, non- and semi-preventable risk factors will maintain cancer prevalence even with successful control of extrinsic factors. (Wu et al., 2018)
Coupled with cancer's intrinsic severity and aggressiveness, these projections inevitably position it as a top cause of death in most modern societies, even in optimistic future health scenarios. Therefore, it should be of especially high priority to not only intensify preventative efforts, but to focus on treatment as well.

Additionaly, it is also crucial to consider that there are already tens of millions of patients either diagnosed with cancer, unknowingly suffering from cancer or in remission. For them prevention is inapplicable as a strategy. Coupled with the challenges to cancer prevention, these facts make reliable diagnosis and successful treatment the more critical stages in the short to medium term.

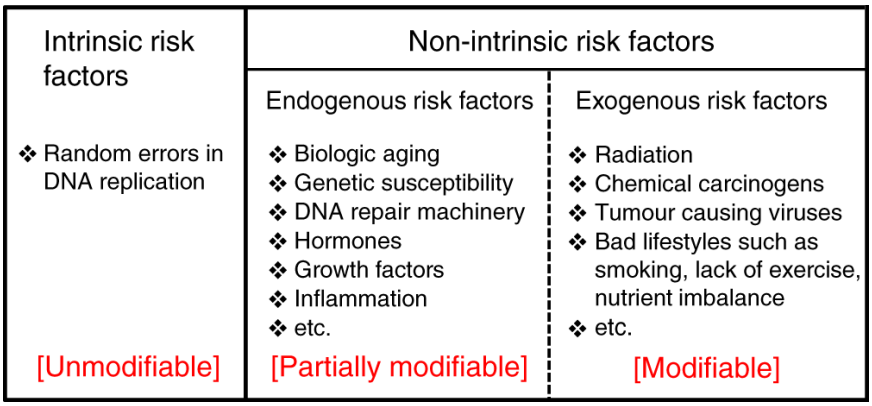

Figure 2: *Risk factors for cancer*
Note: Adapted from "Evaluating intrinsic and non-intrinsic cancer risk factors" by Wu et al. doi:10.1038/s41467-018-05467-z

1.1.2 Early diagnosis and treatment

Early diagnosis is proven to greatly improve the survivability and the quality of life of cancer patients. Nonetheless, this is almost exclusively related to the increased effectiveness of the treatment, when started at an earlier stage of the cancer due to the less weakened immune system, lower tissue infiltration and lower chance of developing metastases. (Miller et al., 2019; Tsai et al., 2018) Effective and selective cancer therapies are especially important after an early diagnosis, as they must be sufficiently cytotoxic to the cancer cells, without damaging the generally healthy organism of the patient. The negative effects of treatment must be minimized to prevent a significant decrease in the quality of life of the patient still in the early stages of the disease. (Rothenberg et al., 2003; Tran et al., 2017)

Overall, an effective and selective cancer treatment builds on the benefits of an accurate early diagnosis and steps in where prevention has failed. As cancer will continue to be a critical health issue for humanity, regardless of successful prevention and diagnosis, efforts for researching and applying effective treatments should continue to be a critical topic of research and development.

1.1.3 Challenges to modern cancer therapy

Developing and applying successful cancer treatments is not without major challenges. Modern oncology offers several treatment methods, all of them with intrinsic benefits and drawbacks to the patient's health. The most suitable one is chosen, depending on the cancer type, the stage of the disease and the patient profile. Surgery, radiation therapy and chemotherapy are the most common approaches, employed separately or alongside others in most cases. (Sung et al., 2021)

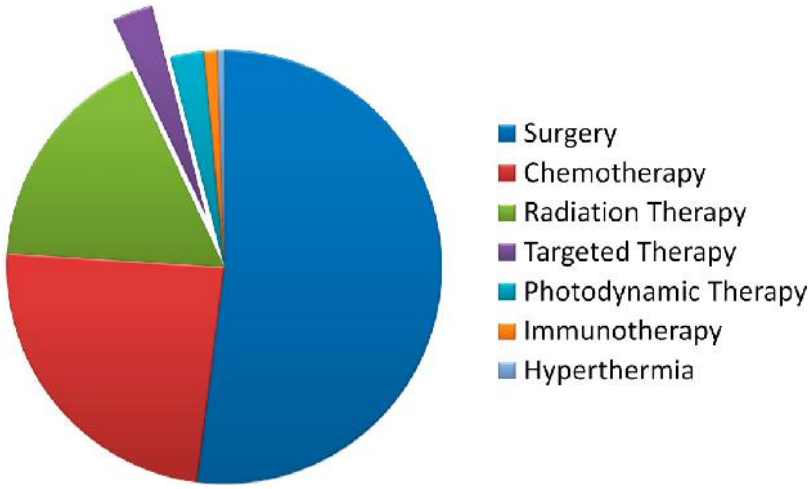

Figure 3: *Relative application of different types of cancer treatment.*
Note: Adapted from "Targeted Radionuclide Therapy of Human Tumors" by Gudkov et al. 2016

Among them, chemotherapy stands out, as it can be effectively used both in standalone and in tandem with other methods. Since it is a minimally invasive procedure, it most often precedes and/or follows surgery and is often used in tandem with radiotherapy. Furthermore, the more effective the chemotherapy gets, the better the chance to avoid surgery altogether. (Skeel & Khleif, 2011; Perry, 2008)

While all current methods of cancer treatment undergo continuous improvement, chemotherapy arguably has the most potential. It relies on the enormous scope of variability and tunability of chemical compounds so the highest relative improvement can be theoretically achieved. For this reason, the field witnessed strong interest by researchers, oncologists and pharmaceutical companies alike.

1.2 Chemotherapeutic agents - the essence of chemotherapy

Chemotherapy as a treatment consists in the administration of one or several compounds that impart a cytotoxic effect on cancer cells, once internalized by them. Depending on the type and structure of the compound, it can affect the cancer cells differently. Several classes of anticancer agents can be distinguished, based on their function in killing cancer cells (Figure 4).

Class	Mechanism	Examples
Alkylating agents	DNA damage, not phase specific	Platinums (cisplatin, carboplatin, oxaliplatin), nitrogen mustard derivatives (cytoxan, chlorambucil), alkyl sulfonates, nitrosourea (carmustine, lomustine), triazines
Anti-metabolites	DNA/RNA replication in S phase of cell division	Pyrimidine analogues (gemcitabine, 5-fluorouracil, capecitabine), methotrexate, gemcitabine-gemzar, 6 mercaptopurine, cytarabine
Anti-tumor antibiotics	Interfere with enzymes needed for DNA replication	Doxorubicin-adriamycin, danorubicin, mytomycin C, bleomycin
Isomerase inhibitors	Interfere with enzymes needed for DNA replication	Topotecan, irinotecan
Mitotic inhibitors	Plant alkaloids that inhibit mitosis in tumor cells	Taxanes-TAXOL, taxotere, vinca alkaloids (vincristine, vinblastine), etramustine - emcyt

Figure 4: *Types of chemotherapeutic agents, based on their function*
Note: Adapted from Chemotherapy induced liver abnormalities: An imaging perspective by Sharma et al., 2014 doi:10.3350/cmh.2014.20.3.317

Regardless of the mode of action, it is generally accepted that the more effective the compound is at killing cancer cells, the more effective the overall treatment. However, alongside its antitumor effects, most anticancer drugs also exert several unwanted toxic effects on healthy tissues. (Hauner et al., 2017; Monsuez et al., 2010) Chemotherapeutic agents, such as paclitaxel (PAX), camptothecin (CPT) and doxorubicin (DOX) are known to cause both long- and short-term side

effects related to heart, kidney, lung and nerve damage. The poor bioavailability, rapid clearance and non-selective tissue distribution further take away from the effectiveness of the treatment and contribute to the severity of the side effects.
Considering these issues, modern chemotherapy aims to develop treatments that maximize the cytotoxic effect on cancer cells while minimizing or preventing any effect on all other cells in the body. This can be achieved through an efficient distribution of the drug only in the cancer-affected tissues and highly selective targeting of cancer cells. (Bor et al., 2019; Li et al., 2017)

1.3 Economic constraints and development considerations

Importantly, for tackling a global health problem such as cancer, developing treatment strategies should not be evaluated “in a scientific vacuum”. To be applied successfully worldwide (to reach the most patients in need) treatments must not only be medically effective, but economically viable. The research and development of novel chemotherapeutic agents involves high costs, long duration and high uncertainty of success, accompanied by the administrative burdens related to the testing and approval process of any successful candidates (Figure 5). Therefore, any novel chemotherapeutic agents are unlikely to be widely applied in the recent future. (Howards et al., 2015) Attempts of modifying already approved anticancer drugs to improve their pharmacokinetics has often resulted in loss of effectiveness or insufficient improvement of their properties to warrant any commercial interest. (Sriram et al., 2004, Rose et al., 1997) Achieving even a highly superior modification still retains the high costs of clinical testing and the uncertainty of approval. Nonetheless, overcoming the limitations of already established anticancer drugs can be achieved without any structural modification, utilizing specialized drug carriers. Drug carriers serve as a shuttle for the chemotherapeutic agent, transporting it into the tumor tissue and into the cancer cells, where it is released, while shielding healthy tissue and cells from its effects. Using approved anticancer agents avoids the need for the lengthy and uncertain target hit and lead identification stage for novel APIs, while still allows for a considerable increase in effectiveness, through improved bioavailability and selectivity due to the shuttle effect of the drug carrier.

Furthermore, using drug carriers in tandem with APIs produced through extraction from limited sources, such as some species of plants and fungi, which is the case of several anticancer therapeutics, can reduce costs related to process intensification and allow for wider application of the treatment. (Greenwell & Rahman, 2015) This comes without an increased risk of medication shortages, as seen in the past, since the scarce API is utilized more efficiently, rather than extracted in higher quantities, allowing for a greater effect per dose and consequently production of more doses.

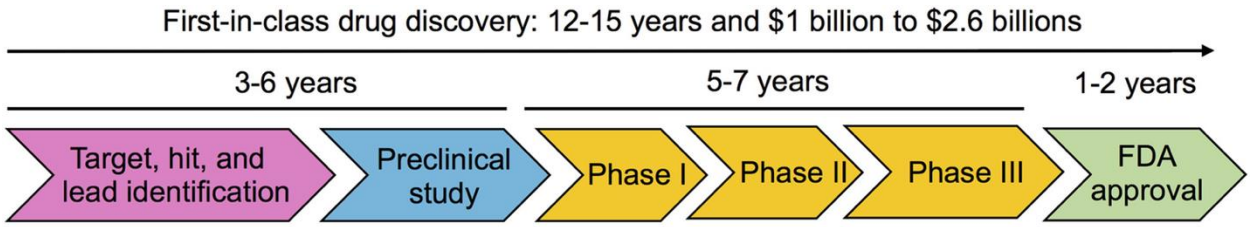

Figure 5: *The development, trial and approval process for novel APIs, average timeframes and cost*
Note: Adapted from doi: 10.1007/978-1-4939-8868-6_15

1.4 Nanometric carriers for chemotherapeutic agents

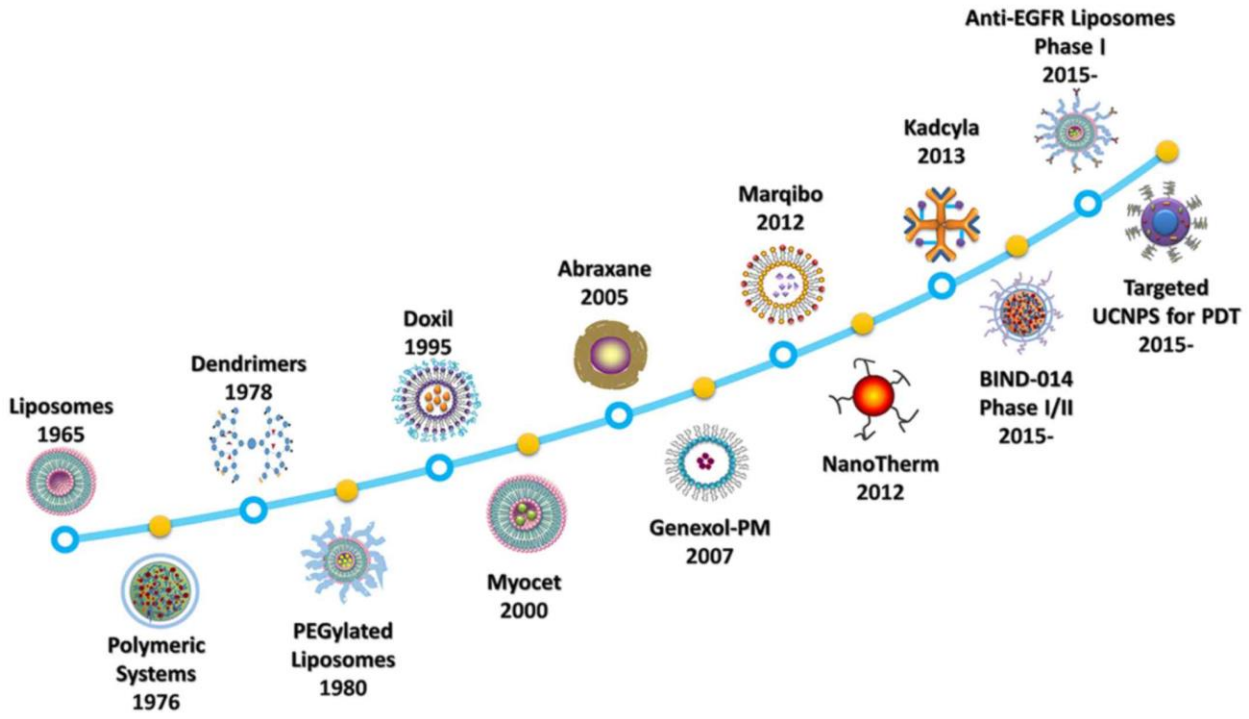

Figure 6: *The development timeline of nanoparticle (NP) drug carriers for chemotherapeutic agents*
Note: Adapted from https://doi.org/10.3892/or.2017.5718

Among the various drug carriers for chemotherapeutic agents (hydrogels, microspheres etc), nanoparticles (NPs) stand out, as they can afford considerable improvement to the bioavailability, selectivity and overall effectiveness of classic chemotherapeutic agents like PAX, DOX, CPT. (Li et al., 2017) The nanomedicine field has enjoyed strong interest in the past years with several developments reaching clinical studies and some even the clinically approved status, such as Doxil – a nanoformulation of DOX encapsulated in liposomes, Abraxane – PAX bound to albumin nanoparticles and Genexol-PM (approved in South Korea) – a polymeric nanomicelle encapsulating PAX (Figure 6).

1.4.1 Advantages of NPs as carriers for chemotherapeutic agents

Apart from their considerable positive effects on drug bioavailability, circulation time and reduced side-effects, NP drug carriers offer several considerable practical advantages. The synthesis of NP could be more straightforward and accessible than the production of many anticancer APIs, especially new-generation agents requiring complex post-synthetic functionalization. Therefore,

improving the pharmacological profile of the drug might be more readily achieved, through incorporation into smart carriers rather than a complex chemical modification process. (Kumari et al., 2014; Park & Na, 2015)

NP formulations also largely resolve the issue of prolonged and intensive administration procedures for many anticancer treatments. Indeed, many biocompatible materials can be utilized at a nanoscale, at which the foreign-body immune response is almost completely avoided, and the nanoparticles can readily be internalized by cells. (Szeto & Lavik, 2016) Currently, many treatment procedures involve highly toxic solvents (e.g., Cremophor EL for paclitaxel) responsible for many of the treatment side effects. Others rely on long and repeated administrations (lasting hours for several days), which cause pain and bruising at the administration site and contribute to the overall mental and physical fatigue of the patients. In contrast, nanoparticles can be administered in saline solutions intravenously, subcutaneously, through mucous membranes or even directly at the tumor site depending on the specific requirements and the therapeutic system. This provides flexibility to achieve higher drug bioavailability for various pathologies (locations and types of tumors) and the greatly reduced toxicity during administration significantly improves patient comfort and quality of life. (Perry, 2008; Mangal et al., 2017)

NPs can be almost endlessly fine-tuned to the specific target requirements. Since the already proven anticancer agents are responsible for the therapeutic effect, modification of the carrier is not limited by the drug-target interaction. Therefore, the structure and composition of the NPs can be tailored to best suit its transport functions with the help of all advancements of synthetic chemistry and biochemistry. Biocompatibility, non-immunogenicity, and safety are essential characteristics of a drug carrier; once these are established, the carrier can be designed according to the specific physiology of the cancer type, the physicochemical properties of the therapeutic agent used and any other pharmacological considerations.

Active targeting is one such modification that utilizes the wide range of functionalization options for NP drug carriers to achieve considerable improvement of selectivity, a significant increase in the cytotoxicity and a better safety profile, in comparison with conventional chemotherapeutic agents. It involves the surface functionalization of the carrier NPs with targeting ligands such as specific peptides, hyaluronic acid, folic acid, antibodies or antibody fragments etc. The targeting ligands allow for specific interaction with surface receptors on the cancer cells and preferential internalization of the NPs. The approach still requires clinical verification and is not applicable to all cancer pathologies. (Pearce &O'Reilly, 2019; Muhamad et al., 2018)

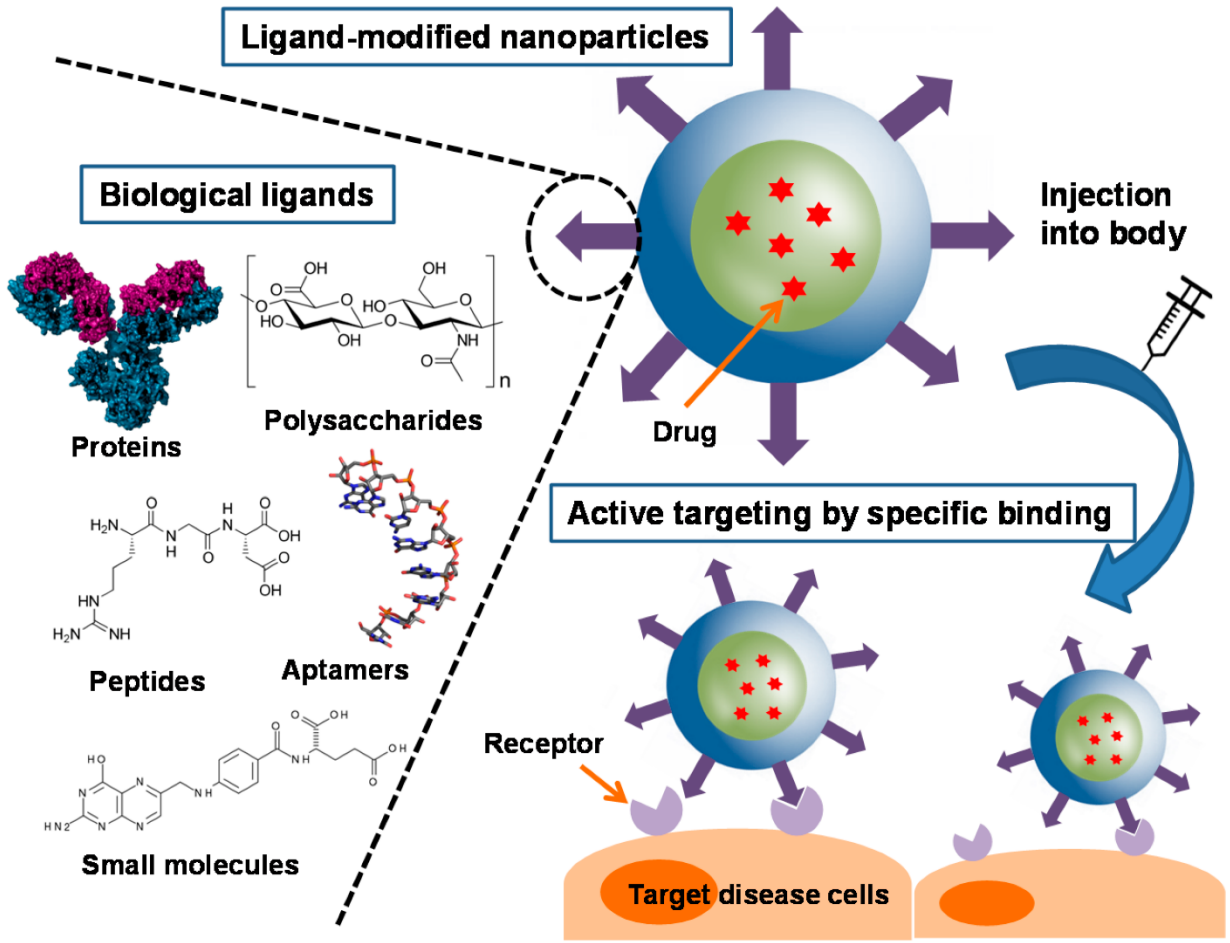

Figure 7: Active targeting ligands and their general mode of action
Note: Adapted from: https://doi.org/10.3390/cancers11050640

However, at the base of all successful active targeting systems lies their passive targeting ability, which stands out as the fundamental characteristic of all nanoparticle drug carriers. It allows NPs to accumulate and remain in solid tumors, utilizing the phenomenon of enhanced permeability and retention (EPR). It has been demonstrated that particles with sizes in the nanometric scale (roughly 1-200 nm), circulating in the bloodstream tend to localize in solid tumors. The preferential accumulation of the nanoparticles is due to the large fenestrations and dysregulated angiogenesis characteristic of the tumor site, coupled with its poor lymphatic drainage. Particle size below 200 nm is often quoted as preferential for permeating the disrupted endothelial barrier of blood vessels at the tumor site. (Maeda et al., 2000; Fang et al., 2011)

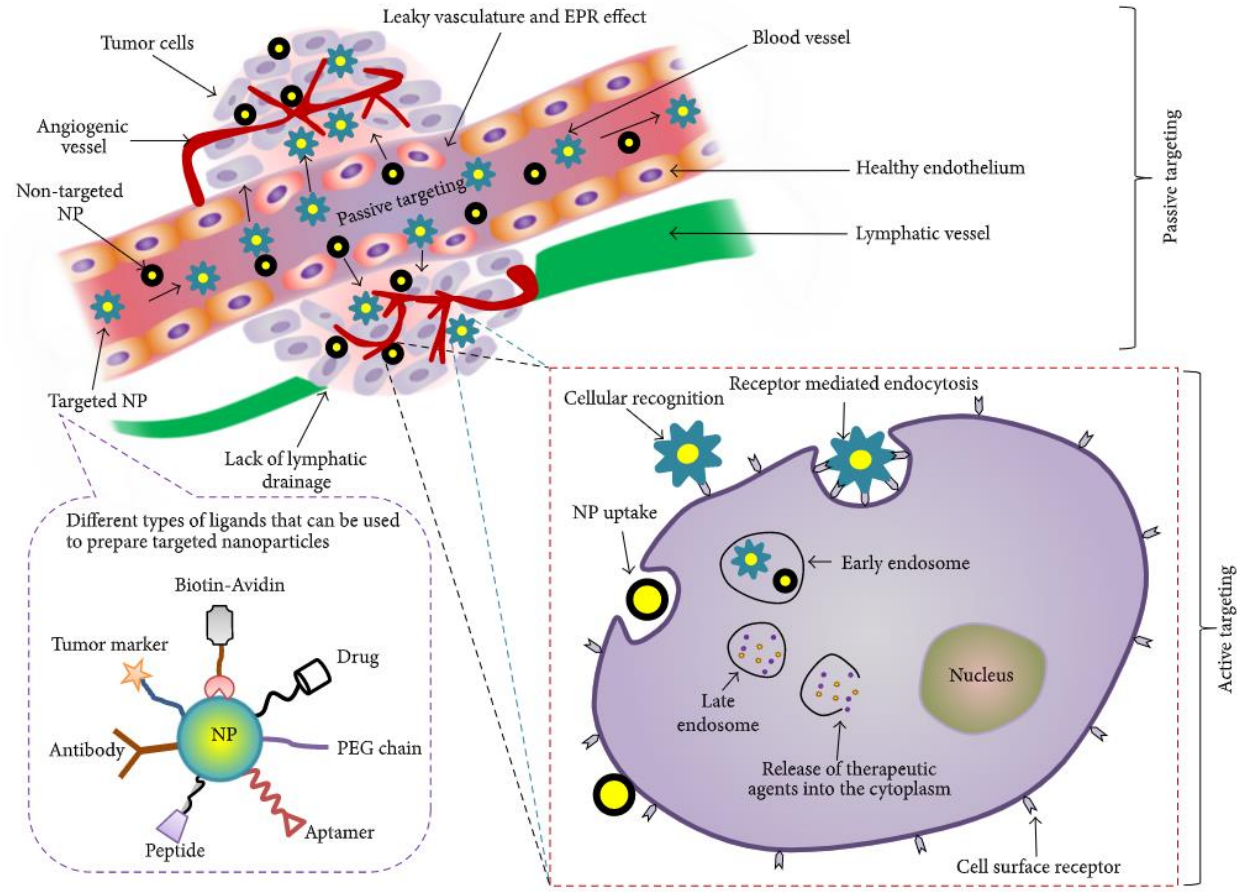

Figure 8: Active targeting and passive targeting (EPR) pathways working in tandem
Note: Adapted from https://doi.org/10.1155/2017/9090325

1.4.2 Photodynamic therapy (PDT)

PDT relies on the selective accumulation of light-sensitive chemical compounds (photosensitizers - PS) in the tumor cells. PS, like chemotherapeutic agents, can exert cytotoxic effects on the cancer cell, once introduced within the tumor. Hence, like chemotherapy, PDT can benefit from the advantages of nanometric drug carriers. A significant difference, however, is that PS are activated only upon light irradiation, which makes PDT more selective than classic chemotherapy. Upon light excitation (usually wavelengths between 500-800 nm) the PS interacts with the diffused oxygen resulting in the formation of radicals, singlet oxygen and triplet species (Figure 9). In turn, the active species effect a variety of cytotoxic reactions oxidizing a range of biomolecules within the cell, disrupting signaling cascades and enzymatic activity and effecting apoptosis. (Ferreira dos Santos et al., 2019; Deda&Araki, 2015)

Photodynamic therapy is noninvasive and usually has shorter administration times than chemotherapy. It can also be repeated over at the same site several times in a short timespan for increased effectiveness, unlike radiotherapy. It most often leaves minimal tissue damage and does not produce scarring, in contrast to surgery. Furthermore, related costs to both the patient

and the treating institution are lower, in comparison to other therapies. However, due to the limited tissue penetration of light, PDT can only be used for treating shallow tumors. Despite their much milder nature, unwanted side-effects are still prevalent, such as untargeted PS accumulation in skin and eyes, in turn inducing long-lasting photosensitivity, especially after systemic administration. This requires patients to avoid sunlight and strong artificial light for weeks, reducing their quality of life. Other side effects include pain and inflammation at the site of irradiation. In recent years, research has focused either on developing more effective PS or, as for chemotherapeutics, producing NP-loaded PS to improve their bioavailability and selectivity towards cancer cells, thus transforming PDT into established next-generation cancer therapy. (Ferreira dos Santos et al., 2019; Deda&Araki, 2015)

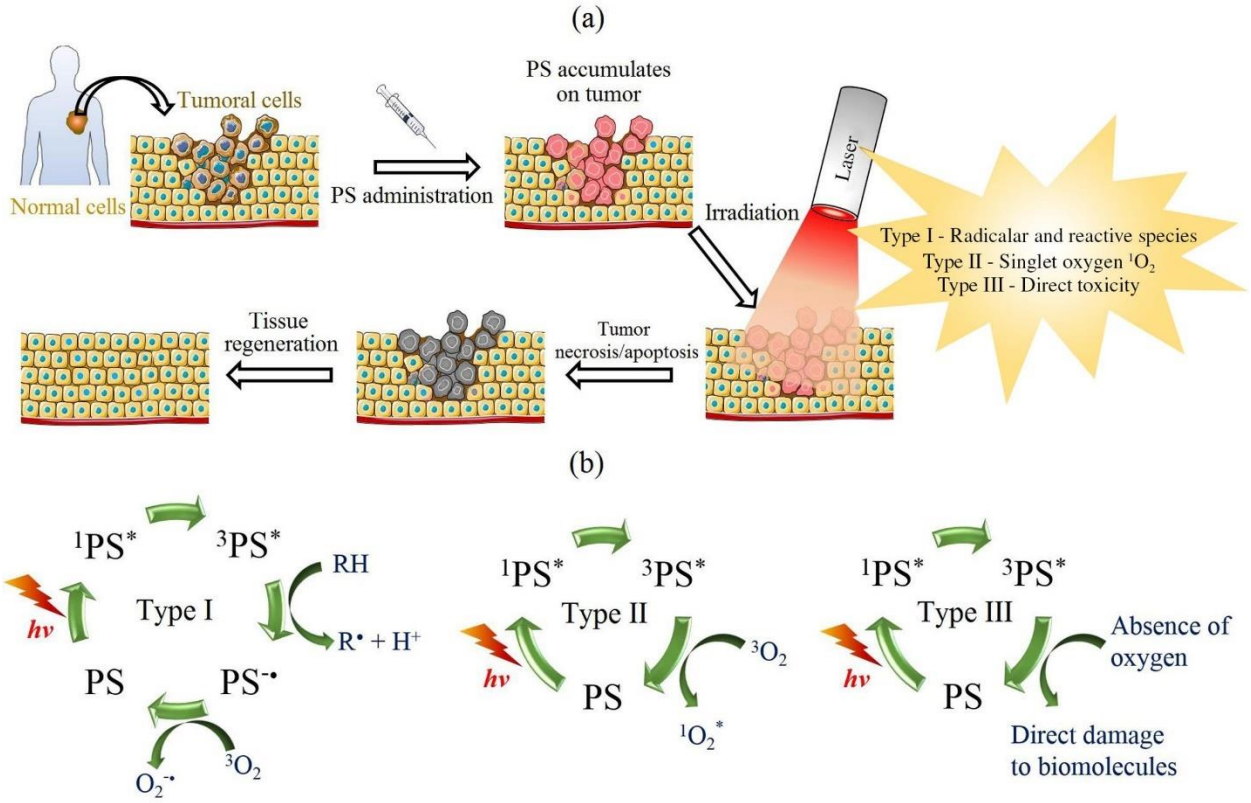

Figure 9: PDT mode of action (top) and mechanism for radical generation from the PS (bottom). Note : Adapted from https://doi.org/10.5935/0103-5053.20150316

1.4.3 Challenges for NP drug carriers (PMMA and core-shell PMMA)

Despite their many advantages, NP drug carriers, depending on their type and composition, can have several shortfalls and drawbacks. The premature drug release during blood circulation accompanied by the nonspecific accumulation of the encapsulated drug in normal tissues is among the most common issues reducing the effectiveness of NP drug carriers and preventing their therapeutic use. (Melancon et al., 2012; Desai, 2012) Poly-methyl-methacrylate (PMMA)

NPs pose a good example for the intrinsic shortcomings of some polymeric nanocarriers. Even though they employ a cheap and biocompatible material that is easy to synthesize and functionalize, PMMA NPs have not proven as effective drug carriers. Due to their neutral charge they tend to aggregate in physiological conditions, rapidly inducing an immune response leading to encapsulation by macrophages, effectively isolating them from their intended target. (Bettencourt & Almeida, 2012; Nel et al., 2009)

Modifying traditional PMMA NPs to have a positively charged surface, retaining the PMMA core, has been found to effectively resolve any agglomeration issues. It further allowed for electrostatic functionalization of the surface of the newly synthesized core-shell NPs (Figure 10). (Monasterolo et al., 2012; Varchi et al., 2013)

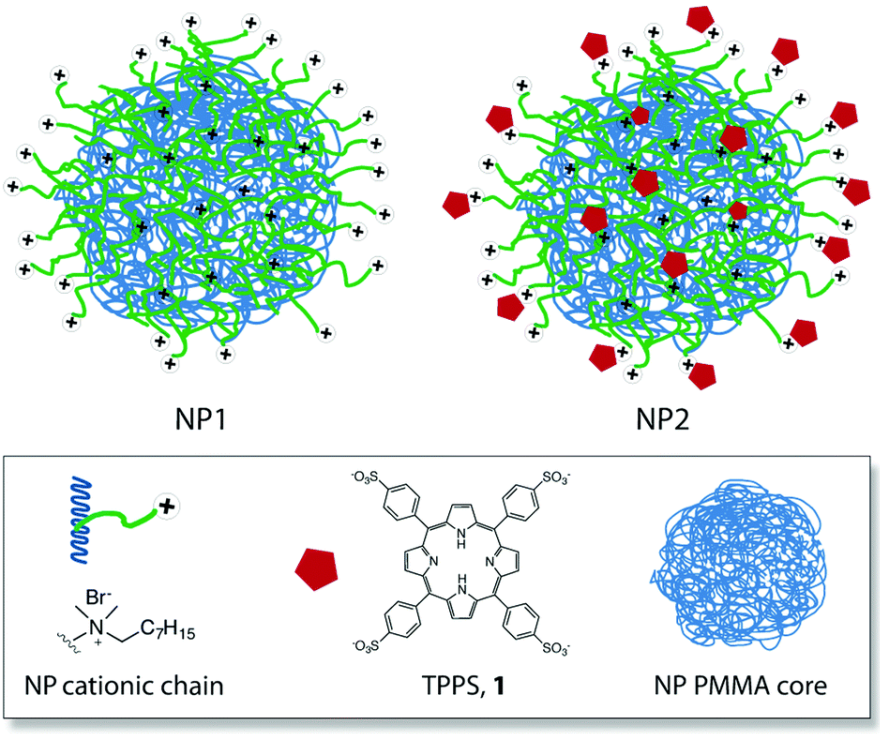

Figure 10: Schematic representation of the positively charged core-shell NP loaded with a positively charged PS.
Note: Adapted from https://doi.org/10.1039/C4GC01996B

Nevertheless, the surface modification procedure, keeping to the nature of PMMA nanometric drug carriers, involved a simple, yet extremely flexible single-step approach. The water-based emulsion radical polymerization involves a polymerizable quaternary ammonium precursor – 2-(dimethyl-octyl) ammonium ethyl methacrylate bromide (TAR) that acts both as the micelle forming surfactant and the charged co-polymer for the methyl methacrylate (MMA) core. The synthesized nanoparticles exhibit better stability and have a strongly positively charged surface which allows for improved internalization through the cell membrane. (Nel et al., 2009; Varchi et al., 2013).

Furthermore, the use of a methacrylate-based radical polymerization co-polymers allows for a large variety of synthetic approaches, such as the incorporation of prodrug functionalized MMA on the surface or as seen in the research of Fraix et al (2015) - the incorporation of photo/sonosensitizers and NO-releasing moieties on the nanoparticle surface. This approach further illustrates the synthetic flexibility polymeric (PMMA in particular) NPs have as drug carriers. Also, the hydrophobic PMMA core of the nanoparticle could carry lipophilic compounds, independently of the electrostatic or covalent load of the surface. (Sahu et al., 2018) This effectively allows for the core-shell NPs to be converted from a drug carrier into a standalone multifunctional therapeutic agent.

1.4.4 Limitations of the PMMA core-shell system

Further studies and development on nanometric drug carriers for anticancer applications have highlighted several limitations of this promising core-shell PMMA system. Monasterolo et al (2012) has demonstrated that the sulfone derivatization of several chemotherapeutic agents, required for their electrostatic loading onto the NPs, significantly decreases their anticancer activity. Also, the strong electrostatic interaction hinders their release, further decreasing their effectiveness. It has been established that passive targeting, relying on the EPR effect, is insufficient as a primary strategy for selectivity as some tumors do not exhibit EPR behavior. Furthermore, the permeability of blood vessels around and within the tumor may not exhibit uniform fenestrations and overgrowth, limiting access to some areas requiring treatment. (Nel et al., 2017)
Importantly, as the PMMA NPs are not biodegradable, they must be excreted from the body, which could pose a risk of accumulation in several organs (liver, spleen, kidneys) and is generally undesirable for future therapeutics. (Tröster et al., 1990; Tröster et al., 1992; Araujo et al., 1999)
To overcome these limitations, the synthetic flexibility of the already proven system can be utilized to impart selective-targeting and biodegradable properties. Several studies have successfully demonstrated that the tumor microenvironment can effectively be exploited as a source both of suitable degradation conditions and specific drug release.

1.5 How to take advantage of the tumor microenvironment

The tumor microenvironment (TME) is found to differ significantly from normal tissue. The super active cancer cell metabolism, the overexpression of several growth factors and the overall morphology of tumor tissue cause large changes in nutrient supply, oxygen diffusion and the overall chemical environment inside the tumor (pH, ROS prevalence, enzymes). More notably, it was established that the concentration of GSH (~ 2-10 mM) is at least 4 times higher in tumor tissue, compared to normal tissues. Importantly, the cytosol level of GSH even for normal cells is significantly higher than that of extracellular fluids (~2–10 μM). This offers a significant redox gradient to be exploited for selective drug release from nanometric carriers, which upon exposure to the high-GSH levels would release their drug cargo and biodegrade.

In view of this strategy, various redox-responsible nanometric delivery systems have been developed and described. Most of them impart redox sensitivity to NP structure through the incorporation of disulfide bonds. Upon introduction in an environment with a high GSH concentration, the disulfide bond is cleaved into two sulfhydryl groups, oxidizing GSH in the process. (Wang et al., 2017; Deng et al., 2015) This reaction normally involves protein disulfide bridges and is part of the natural metabolic pathways of cells. Incorporating disulfide functionality usually takes place through crosslinkers or pendant copolymer residues. Several studies have demonstrated the ability of disulfide-containing polymeric nanoparticles to selectively release covalently attached chemotherapeutic agents in a reducing environment. (Khorsand et al., 2013; Cho et al., 2012; Deng et al, 2015) To our knowledge, none of those include complete degradation of the carrier as a result of the disulfide cleavage and most of those are specific to a single therapeutic agent. Furthermore, most synthetic procedures involve a multitude of steps and potentially expensive or exotic reagents.

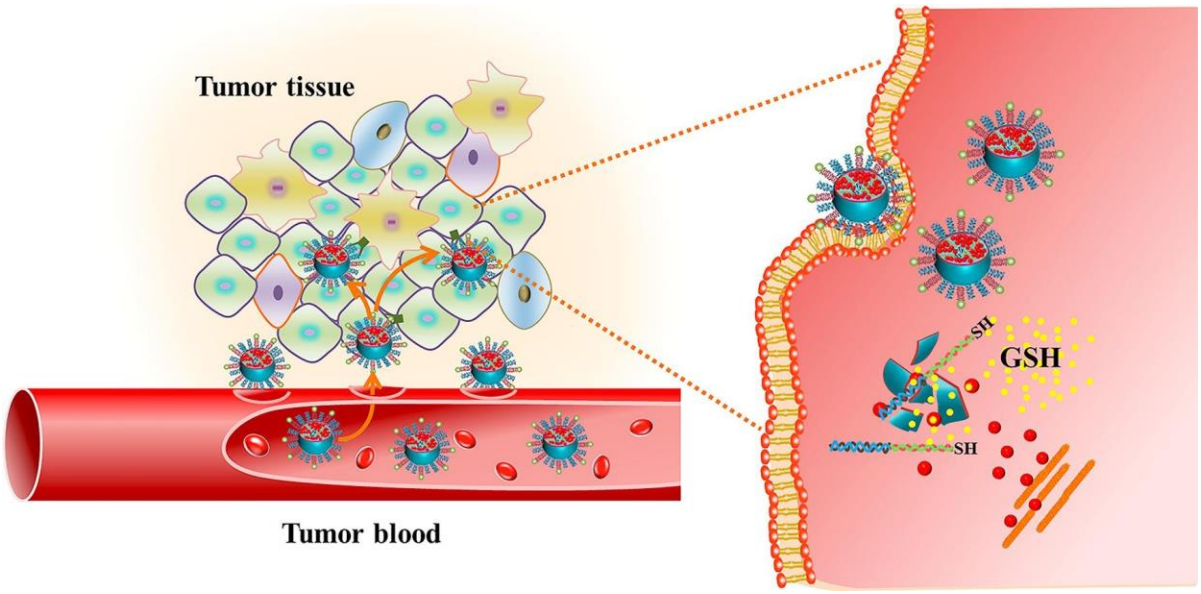

Figure 11: Redox-sensitive NPs interacting with the tumor microenvironment at elevated GSH levels
Note: Adapted from https://doi.org/10.1016/j.ijpharm.2018.09.050

1.6 The philosophy behind the studied system – aim of the thesis

The principal idea behind the present study is to conserve the simple and effective synthetic procedure and the proven structure of the core-shell PMMA nanoparticles, while introducing redox-cleavable functionality. Utilizing an already proven redox-responsive crosslinker - Bis(2-methacryloyl) oxyethyl disulfide (DSDMA), as a main building block is expected to fulfil those requirements. The extra polymerizable methacrylate moiety can potentially introduce morphological changes to the nanoparticles. However, using it as the principal monomer is the only way to introduce degradable links in the body of the polymeric NP and not just as a pendant. The emulsion polymerization process would be performed via the same surfactant (TAR), proven to effectively work with a methacrylate-based monomer (MMA). It is, therefore, expected that the charged surface-properties of the resulting disulfide-polymethacrylate NPs would resemble those of the original PMMA core-shell system, retaining the ability for electrostatic coordination of molecular cargo.

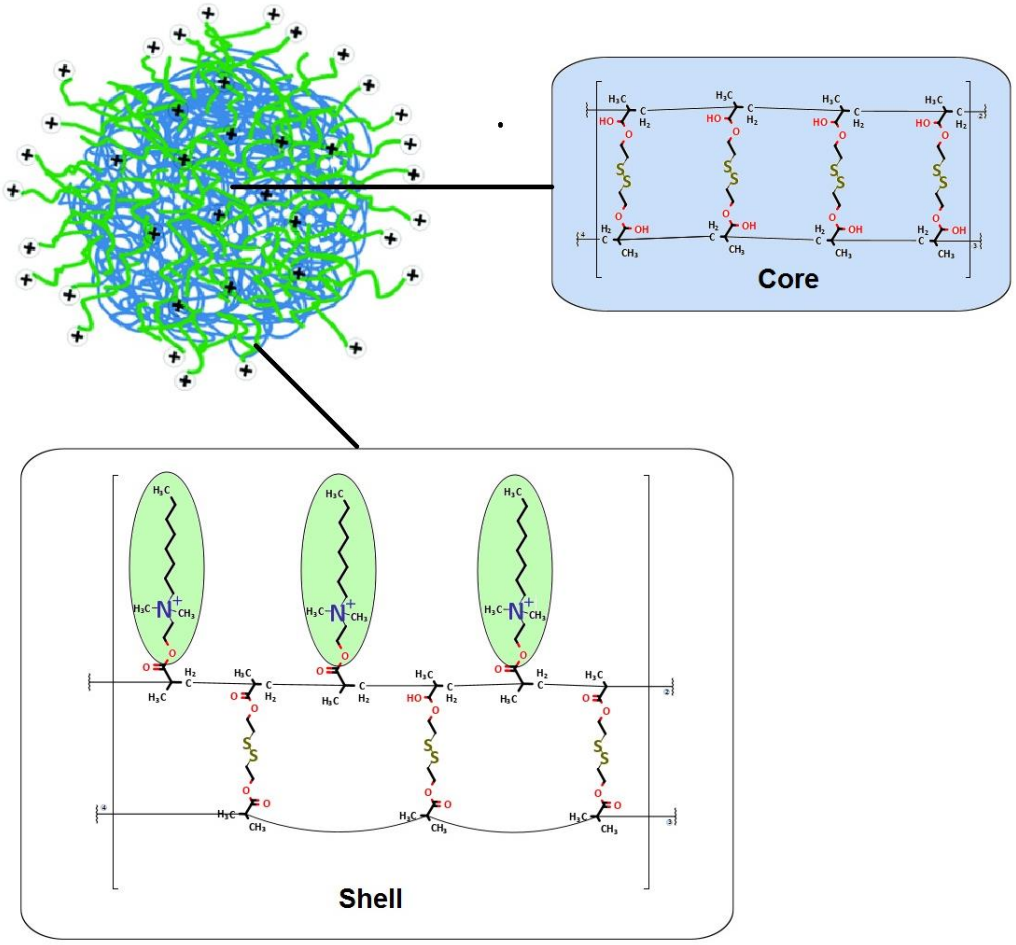

Figure 12: Schematic of the expected structure and composition of the disulfide-containing core-shell nanoparticles.

The goal of the research was to synthesize and study a biodegradable stimuli-responsive drug carrier, based on positive core-shell PMMA nanoparticles for chemotherapeutic applications. It was expected that the DSDMA precursor, as a drop-in replacement for MMA, would allow for the synthesis of core-shell polymethacrylate-based NPs, containing disulfide linkages within their main chain structure and a positively charged surface. The synthesized NPs were expected to retain the (surface) functionality of the original PMMA-based NPs, while being degradable at reducing conditions. It was expected that the synthesized NPs would be suitable as a potential drug carrier for chemotherapeutic applications.

2 Materials and methods

2.1 Materials and characterization

Reagents, solvents and auxiliaries were purchased from Sigma Aldrich/Merck - Methacryloyl chloride (MAACl), Methacrylic anhydride (MAAnh), 2-Hydroxyethyl disulfide (HEDS), 4-Dimethylaminopyridine (DMAP), Triethylamine (TEA), Dichloromethane (DCM), Ethyl acetate, Hexane, 2,2′-Azobis(2-methylpropionamidine) dihydrochloride (AIBA), methyl methacrylate (MMA). The ionic comonomer and reactive tensioactive 2-(dimethyl-octyl) ammonium ethyl methacrylate bromide (TAR) was previously synthesized as described in literature (Laus et al., 2000; Varchi et al., 2013). Ultrapure water was produced using a Sartorius Arium Pro® system (Sartorius, Monza, Italy).

Crude products were purified by flash chromatography using silica gel (0.037-0.063 mm, Merck) as a stationary phase; solvents were distilled according to standard procedures. Analytical thin-layer chromatography was performed on Merck Kieselgel 60 F254 silica gel plates and visualization was accomplished with $KMnO_4$ or Pancaldi solutions.

Compounds were characterized at room temperature with Nuclear Magnetic Resonance spectroscopy (NMR) using a Varian MERCURY- 400 (400 MHz) spectrometer or on an Agilent NMR DD2 (500 MHz) in deuterated chloroform, unless otherwise stated. Hydrodynamic diameter and polydispersity index (PDI) of NPs was determined by dynamic light scattering (DLS) analysis at 25 ◦C using a NanoBrook Omni Particle Size Analyzer (Brookhaven Instruments Corporation, USA) equipped with a 35 mW red diode laser (nominal wavelength 640 nm).

Thermogravimetric analysis (TGA) was performed on a Perkin Elmer TGA 4000 and spectrophotometric measurements were done on a Cary 100 Uv-Vis spectrophotometer (Agilent Technologies, USA). A DLAB D3024 centrifuge and Merck Amicon™ Ultra-0.5 Centrifugal Filter Units (Merck, USA) were used for the filtration of PS-loaded NPs for the ROS activity tests.

2.2 Precursor synthesis

DCM was distilled from Magnesium and kept under molecular sieves before use for the reactions. All reactions on the precursor synthesis were performed in anhydrous conditions, under nitrogen.

2.2.1 Synthesis via the MAACl pathway

2,23 g (14,5 mmol, 1 eq) of HEDS was added to 50 mL of DCM, forming a suspension. Subsequently, 3,2ml (43,1mmol, 3 eq) of anhydrous triethylamine (TEA) were added to the

solution and the flask was placed in an ice bath. 3,03 ml (29 mmol, 2 eq) of MAACl were added dropwise, while the solution was kept on ice. The reaction was then maintained at 0°C for 40 min followed by further 4 h at room temperature. 70 mL of saturated ammonium chloride solution was used to quench the reaction, and the resulting mixture was transferred into a separatory funnel and extracted with DCM (2x70 ml). The collected and combined organic fractions were washed with water and brine (2 x 70 mL). The resulting organic fractions were dried over anhydrous sodium sulfate, filtered and solvent removed with a rotary evaporator. The resulting viscous pale yellow oil was separated via flash column chromatography on silica with 1:6 ethyl acetate:hexane. The process yielded 1,89g (6,5mmol, yield:45%) of pale-yellow oil.
^{1}HNMR (400 MHz, $CDCl_3$, δ, ppm): 1.95 (s, 6H, -CH3), 2.96-2.99 (t,4H, -S-CH2-), 4.39-4.43 (t, 4H, -O-CH2-), 5.59 and 6.13 (s,4H, CH2)

2.2.2 Synthesis via the MAAnh pathway

2,23g (14,5mmol, 1 eq) of bis-hydroxy-ethyl-disulfide was added to 50 mL of DCM, forming a suspension. Subsequently, 0,353g (2,89 mmol, eq 0,2) of DMAP were added to the solution. 6,63g (43,1 mmol, 3 eq) of MAAnh were added dropwise. The reaction was kept overnight at room temperature. 70 mL of water was used to quench the reaction, and the resulting mixture was directly transferred into a separatory funnel. The organic layer was washed with 0.1M NaOH, water and brine (2x 70 mL each), and each aqueous fraction was extracted with 50 mL of DCM. The resulting organic fractions were dried over anhydrous Na_2SO_4, filtered and solvents removed with a rotary evaporator. The resulting viscous pale yellow oil was separated via flash column chromatography on silica with 1:6 ethyl acetate:hexane. The process yielded 2,64g (9,1mmol, yield:63%) of pale-yellow oil. ^{1}HNMR (400 MHz, $CDCl_3$, δ, ppm): 1.95 (s, 6H, -CH3), 2.94-2.99 (t,4H, -S-CH2-), 4.38-4.41 (t, 4H, -O-CH2-), 5.59 and 6.13 (s,4H, CH2)

2.3 NPs synthesis and purification

Ultrapure water was used exclusively for all reaction and purification procedures. All polymerization reactions were kept under nitrogen atmosphere

2.3.1 TAR method (MMA copolymer)

10 mL of water in a 25 mL three-necked round-bottomed flask were purged with N_2. 110 mg (0,33 mmol) of TAR were dissolved under stirring. The chosen monomers were premixed and introduced into the solution. Various amounts and ratios of monomers were used from 100 to 400 µl in total (see Results and discussion section). Afterwards the solution was heated to 80 °C in an oil bath under reflux. 16 mg of AIBA were dissolved in 200 µl of water and introduced in the reaction solution. The reaction was maintained for 4h at 80 °C. Afterwards the solution was opened to air and cooled to rt, and then filtered through cotton if aggregates were visible, and transferred into a dialysis bag for further purification.

2.3.2 Cetrimonium bromide-assisted (CTAB) method

Nanoparticle synthesis using CTAB as a surfactant followed the previously described procedure. An additional step of adding 45 µl of CTAB water solution (23,2 mg/ml) alongside the addition of TAR was performed. Also, in some cases, the reaction solution was sonicated before the addition of AIBA and lower amount of TAR was utilized.

Table 1: Reagent amounts and auxiliary procedures used for the synthesis

NP name	DSDMA (mg)	MMA (mg)	TAR (mg)	AIBA (mg)	Comment
RefMMa		374,00	116,00	10,60	MMA-only reference
MASS210	210,00	188,00	109,40	12,90	
SS450	456,00		106,00	17,00	
MASS100	100,30	300,80	105,00	16,00	
SS114	114,00		115,00	20,00	Reduced DSDMA amount
CTABSS1	140,00		21,00	13,30	CTAB-assisted
CTABSS2	150,00		21,70	15,00	Sonicated and CTAB-assiste
SS114NR	114,00		110,00	20,00	Nile Red cargo
CTABMA		374,40	21,00	13,30	CTAB-assisted MMA reference
CTABSS3	114,00		114,00	20,00	CTAB-assisted high-TAR loading

2.3.3 Dialysis and pressure filtration

Primary purification of the synthesized nanoparticle solutions was performed with dialysis. The solution was poured into a 12 kDa bag and placed in 400 mL of water. The water was changed periodically, and its conductivity was measured before every change. When a stable value for the conductivity was observed (over 3 water changes), the NP solution was transferred to a pressure filtration apparatus (Amicon 8050 Stirred Cell). The NP solution was then further purified by washing with water through a filter (100 kDa). Aliquots of filtrate were collected at the beginning of the process and after every 100 ml of filtrate and analyzed with UV-Vis spectrophotometry (Cary 100, Agilent Technologies). The procedure was stopped after the aliquots showed diminished absorbance at ~210nm (<0.2), indicating the lack of contaminants. The resulting solution was diluted to a total volume of ~ 15 mL and transferred to a polypropylene container for storage and further experiments.

2.4 Rotary evaporation (yield)

The concentration of the NP solutions was measured by weighing the dry content of 300 μl of solution. Dry NPs were obtained by vacuum rotary evaporation overnight (centrifuge equipped with a liquid nitrogen trap). The procedure was made in quadruplicate for each NP solution. The following equation was used to obtain the NP concentration in the stored solutions:

$$\frac{\sum weight\ sample/0.3}{4} = NP\ concentration$$

The following equation was used to calculate the yield of the NP synthesis reaction:

$$\frac{DSDMA(mg)+MMA(mg)+TAR(mg)+AIBA(mg)}{NP\ concentration*Vsolution} * 100 = NP\ \%yield$$

The dried NPs were used for TGA characterization.

2.5 NPs characterization -

2.5.1 DLS

The hydrodynamic diameter of the nanospheres was determined by photon correlation spectroscopy (PCS) at 25 °C using a NanoBrook Omni Particle Size Analyzer (Brookhaven Instruments Corporation, USA) equipped with a 35mW red diode laser (nominal 640 nm wavelength). Data were analyzed using the viscosity and refractive index of pure water at 25 °C. The instrument was calibrated with standard polystyrene latex particles of 200 nm in diameter. ζ-potential was measured at 25 °C by means of the same system. The instrument calibration was checked using standard polystyrene latexes, supplied by Brookhaven Instruments Corporation with known ζ-potential.

2.5.2 TGA

TGA measurements were performed on a Perkin Elmer TGA 4000. The fully purified solutions of the synthesized NPs were utilized as samples (except for CTABSS1 and CTABSS2). Agglomerated NPs were only purified through dialysis the bulk residues were scraped directly from the reaction flask. All samples were dried via rotary evaporation with a cold trap, overnight, prior to analysis. Samples ranged from 1 to 4 grams. The following TGA method was used for all samples: Initial temperature - 30 °C, final temperature 600 °C; achieved through a 10 °C/min linear temperature ramp. Nitrogen purge flow was set to 30ml/min throughout the entire run. Data from the analysis was exported with the instrumentation software (Pyris, Perkin Elmer), while consequent derivatization and smoothing (moving average, 20 datapoints window) was

performed with Oirigin (OriginLab Corporation) data processing software. Peak identification was done manually by correlating the lowest weight loss values at the beginning and end of the specific peak to the corresponding % weight and sample temperature.

2.5.3 Argentometric(Ag) titration

The loading per gram of nanospheres of primary and quaternary ammonium groups was determined by potentiometric titration of the chloride and bromide ions respectively obtained after complete ion exchange. The ionic exchange was accomplished by dispersing 67.5 mg of the nanosphere sample in 25 ml of 1 M KNO3 at room temperature. The mixture was then adjusted to pH 2 with dilute H2SO4 and bromide and chloride ions were titrated with a 0.0201 M solution of AgNO3. The resulting mqmol/g results were transformed to %wt values for ease of comparison to synthesis and TGA data. The transformation was done through the equation below and the resulting value represented the wight percentage of TAR located on the surface relative to the entire weight of the NP:

$$\frac{Titration\ value * TAR\ MW}{1000000} * 100 = TAR\ \%wt$$

2.6 Properties studies

2.6.1 DTT degradation

Aliquots from the available purified NP solutions were taken and diluted to a concentration of 4mg/ml, forming stock solutions. 750μl of a previously prepared 12mM solution of Dithiothreitol (DTT) was added to 250μl of the stock NP solutions to yield final tests solutions with a NP concentration of 1mg/ml and a 8,7mM concentration of DTT.
The test solutions were kept at room temperature on an orbital shaker and monitored through DLS. For the DLS measurements 50 μl aliquots were taken and dissolved in 1,8ml of Ultrapure water at 0h, 2h, 4h, 24h, 48h, 72h, 6d (96h for MASS100) and 7d after the initial addition of DTT.

2.6.2 Reactive Oxygen Species (ROS) production studies

The ROS production of the synthesized NPs was evaluated using the chemical probe 2′,7′-dichlorodihydrofluorescein diacetate (H2DCFDA). The commercially obtained H2DCFDA was dissolved in methanol obtaining a 1.1 mM solution. Two mL of NaOH (0.01 M) were added to 500 μL of the methanolic solution, then shaken and kept in the dark at room temperature for 30 min. Afterwards, 10 mL of phosphate buffer (pH = 7.4) were added providing the final ROS probe solution, which was used for all consequent tests. The ROS probe solution was stored at 8°C with minimal light exposure. (Ferroni et al., 2016)

The Tetrasulfonated Aluminum Phthalocyanine (AlPCs4) photosensitizer was electrostatically loaded on the NPs by introducing 4μl of a 1mg/ml AlPCs4 solution and 18μl of a 28,1mg/ml MASS210 NP solution to 260μl of water and vortexing the mixture for 30sec. The resulting solution was used for preparing the final test solutions. A duplicate was analyzed through centrifugation filtration and UV-Vis spectrophotometry to assess if complete PS loading was achieved.
Final test solutions were prepared by combining the purified NP solutions (both of PS-loaded and unloaded NPs), water, 500μl phosphate buffer (7,4 pH, 20mM) and 220μl ROS probe solution to achieve a total volume of 1ml and a total NP concentration of 0,5mg/ml. Immediately upon addition of the ROS probe, the solution was transferred to quartz cuvette and the ROS test was conducted. Irradiation was performed with a Tungsten lamp (Phillips, 300W). The samples were placed in quartz cuvettes 40 cm away from the light source and were irradiated for 5, 10 and 15 mins consecutively (30 mins total). UV-Vis measurements done immediately after the addition of the ROS probe and after every irradiation interval on a Cary 100 UV–Vis spectrophotometer (Agilent Technologies).

2.6.3 Compound encapsulation studies (Nile red)

All previously described procedures were performed for the synthesis of the Nile red-containing NPs (see TAR method, no MMA was included). Before the addition of AIBA initiator 1mg of Nile Red dye, dissolved in 100μl of DMSO was added to the reaction mixture. All purification and quantitation procedures were then followed as for previously synthesized NPs.

3 Results and discussion

3.1 Precursor synthesis

The precursor is commonly used as a redox-sensitive crosslinker in NP formulations. To our knowledge, it has not been used as the bulk constituent of NPs. This research is the first attempt at using DSDMA as a primary building block for NPs for drug delivery. DSDMA is commercially available as a building block, however, the relatively high price has prompted several researchers to synthesize it (Rosselgong et al., 2009; Poupart et al., 2017; Wang et al., 2014). Furthermore, the synthesis of the singly substituted homolog is well documented in literature and relies on the same starting material (HEDS) and reaction (ester formation). (Deng et al., 2015; Xu et al., 2013)

The DSDMA precursor for this study was synthesized via two separate pathways - through reaction of dithio-ethanol with MAACl and with MAAnh. Both pathways yield the same final product. However, the potential impurities, co-products and side-products vary greatly between the two and require somewhat different purification. Reaction time and conditions also vary between the two, mostly related to the reactivity of the methacrylate moiety. MAAnh synthesis takes place at RT and over the course of 24h, while MAACl reacts to completion in 4 to 6 h and the reaction should be initiated on ice.

In the ideal case, involving brand new reagents, the precursor is afforded in high yield and is easily separated from the monosubstituted compound and the starting material (if any) through column chromatography. However, the presence of impurities greatly increases the difficulty in the isolation of pure precursors, especially in the case of the MAACl pathway. As found by (Warneke et al., 2014) MAACl tends to form several impurities after exposure to moisture and air (during routine laboratory use). Those have been shown to be successfully removed by distillation. However, such a procedure adds extra hazards, labour and losses to the otherwise straightforward synthesis. As found by our work, used (opened) MAACl is essentially unsuitable for the synthesis of DSDMA, as the resulting impurities are extremely hard to separate from the desired product. Moreover, upon storage (2-weeks, air, -20 °C) of the crude mixture, considerable decomposition is observed, evident by TLC and a color change of the sample.

MAAnh, whilst still sensitive to moisture, is less active than MAACl and mostly forms methacrylic acid as an impurity after its first exposure to air. The available MAAnh contained several impurities (as evident by NMR see Appendix Figure 1), but when used for the synthesis and after separation by column chromatography, still yielded sufficiently pure DSDMA. On the other hand, the co-product of the MAACl pathway is TEA•HCl which is often easily filtered out at the start of the purification stage, whilst for the MAAnh pathway, 2 mol of acrylic acid is produced for each mole of DSDMA. This can present a moderate inconvenience, especially at larger quantities, as the MAcid must be removed through large amounts of water and basic solution.

Nonetheless, with the use of pure starting materials, a successful resolution is possible with a straightforward isocratic column chromatography (1:6 Ethyl acetate:hexane). Furthermore, the

intensiveness (how selective/effective) of the purification steps can be shifted between the liquid-liquid extraction and the column chromatography, by modulating the use of excess MAAnh or MAACl. Using stoichiometric amounts of the reagents (2eq.), resulted in the presence of some MAHEDS in the crude mixture, which is separated from DSDMA via the chromatography step. Using excess of the reagents (2.5-3eq) results in a complete conversion of HEDS to DSDMA (and any potential impurities), however, requires neutralization and removal of a larger amount of unreacted MAACl and TEA•HCl or MAnh and methacrylic acid respectively.

We consider this information crucial for practical considerations, as the use of DSDMA as a bulk building block, rather than just a crosslinker, implies the need for larger quantities and several synthesis runs. In such cases, the yield, the crude product composition and the intensity of the purification procedures could become instrumental to the feasibility of the synthetic approach and the timeline of the research.

After all the purification procedures, regardless of the chosen pathway, DSDMA is afforded as a light-yellow oil. The yield varied between 45% and 63%. All synthesis procedures and some of the purification procedures were of explorative, rather than productive nature, therefore, should not be fully representative of the maximum yield potential of the reaction pathways. During storage at -20 °C and occasional exposure to room temperature, the substance remained unchanged in appearance, reactivity and composition (1H NMR) for >2 months, without any addition of stabilizers.

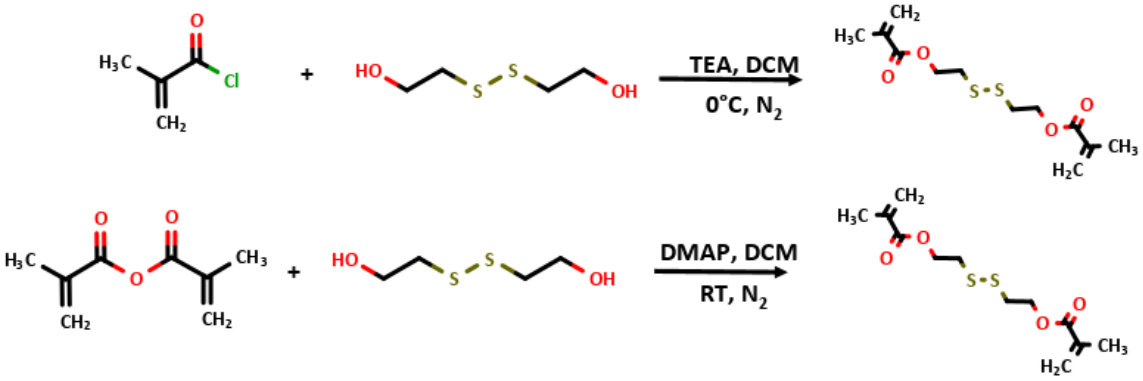

Figure 14: Reaction scheme for the MAACl pathway (top) and the MAAnh pathway (bottom).

3.2 Nanoparticle synthesis

The aim of the NP synthesis section was to establish any changes the addition of DSDMA introduces to the synthesis of core-shell NPs, both as a copolymer to PMMA and as a singular monomer.

The synthesized DSDMA was used as a drop-in substitute for MMA in the emulsion polymerization process used for NP synthesis of the NPs used by Varchi et al. (2013) and Monasterolo et al. (2012). The use of TAR as both an emulsifier and a charged copolymer was again pivotal to produce core-shell NPs. The use of water-soluble AIBA initiator and reaction conditions (N_2, 80 °C, 4h) followed the already well-established procedures from previous research. Initially, three different NPs were synthesized, containing varying amounts of precursor (79 wt%, 40 wt% and 20 wt% DSDMA), and MMA as a copolymer to evaluate the effects of the DSDMA on the composition and properties of the final product. At the start of the synthesis, it was observed that the precursor is not miscible with water, forming a separate layer when introduced in pure H_2O. Upon introduction of TAR and vigorous stirring (600 rpm) a fine emulsion was formed (observed through solution opalescence). After radical initiation, the formation of agglomerates was observed at the air/liquid interface. Additionaly, solid residue was found on the bottom of the flask after the end of the reaction. Inefficiency in the DSDMA emulsification was given as the main reason for the formation of the agglomerates and the residue was attributed to bulk polymerization. Nonetheless, the precursor appeared fully soluble in MMA, facilitating its introduction to the reaction vessel, in the case of the MMA-copolymerized NPs. However, bulk polymerization was still observed by the end of the reaction, albeit to a lower extent.

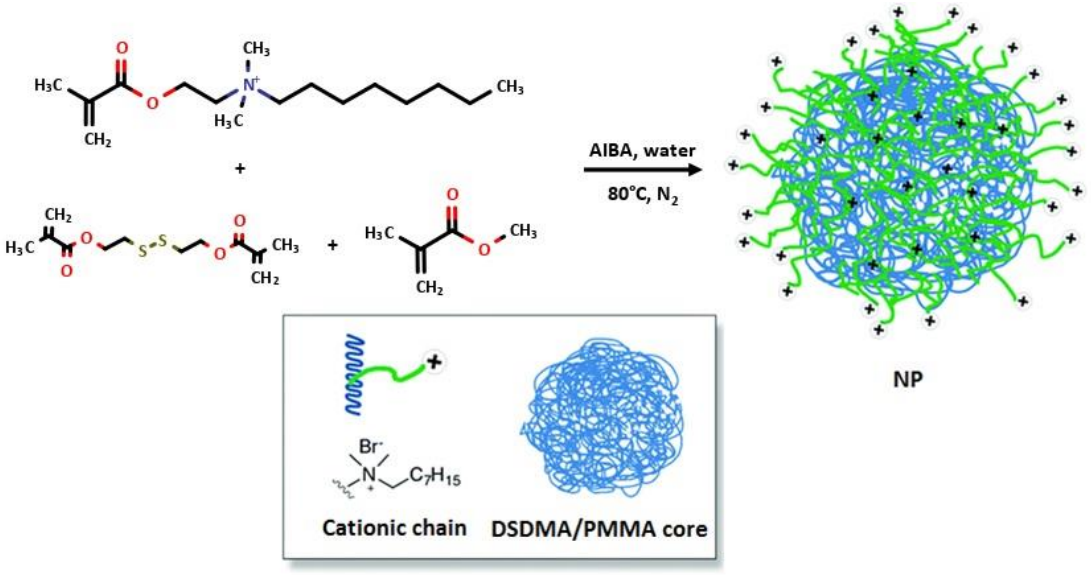

Figure 15: Reaction scheme for the NP synthesis

3.2.1 Nanoparticles purification

After termination of the reaction by exposure to air and cooling, the solution was filtered through cotton, removing the bulk residue and agglomerates and placed into a dialysis tube. The tube, containing the ~10 ml of reaction solution was then placed in 400ml of MilliQ water under slow stirring. The water was replaced every 24 h. The conductivity of the water was measured before each replacement, indicating the amount of soluble compound released by the NPs solution (see Table 2). Through this simple procedure, most of the residual unreacted TAR and unreacted initiator decomposition products, alongside any soluble impurities should be mostly removed. This should facilitate the consequent pressure filtration, reducing the amount of water needed for complete purification of the NPs. After a stable conductivity value was reached, regardless of water replacement (usually after ~5 days), the NP solution was taken out of the dialysis bag. The solution volume was measured and transferred to the pressure filtration apparatus. Measuring the volume of the final solution in the dialysis bag presented another point of reference for the charge of the NPs. NPs that were found to possess a high ζ-potential and higher TAR availability on the surface (through titration), also retained more water during dialysis (more than the initial 10ml of the synthesis solution). Vice-versa, less charged NPs with lower surface TAR loadings, had a reduced amount of water retained in the dialysis bag (<10 ml). NPs that tended to agglomerate (see later) retained less than 4ml of water and visibly formed agglomerates within the dialysis bag.

Table 2: Average conductivity measurements during the dialysis purification step for the synthesized NPs.

	First measurement	**Halfway measurements**	**Final measurement**
Average conductivity (μS/cm)	39-100	5-11	1-3

Pressure filtration was performed with the aim of further reducing the amount of soluble impurities within the NP solution. UV-Vis was used to monitor its effectiveness, by analyzing the permeate water solution. A sufficiently purified sample showed permeate with less than 0,2 A at 200-220 nm, indicating that very low amounts of soluble substances were filtered through. The filtrate solution was then diluted to practical levels (10-20 ml) analyzed for its size, charge and composition and subjected to further tests (degradation and ROS production). The low level of soluble compounds should allow for accurate measurement of the NPs' hydrodynamic diameter (with limited effect of the coordination sphere on the results and ζ-potential (limited effect of coordinated charged species on the surface charge of the NPs).

Furthermore, the most likely targets of the purification - TAR, AIBA decomposition side-products, oligomers and short polymers - would likely affect the composition analysis through TGA. Therefore, such a thorough purification procedure is considered highly necessary. Considering the pore size for the dialysis and for the pressure filtration and the achieved NP diameters, there should not have been any considerable effects on the NP distribution from the purification procedures. Dialysis should not have affected the yield considerably, while pressure filtration

could have - mostly associated with embedding NPs in the filter. Therefore, the purified NPs should be a representative product of the synthesis process and be suitable for a representative analysis and consequent properties tests.

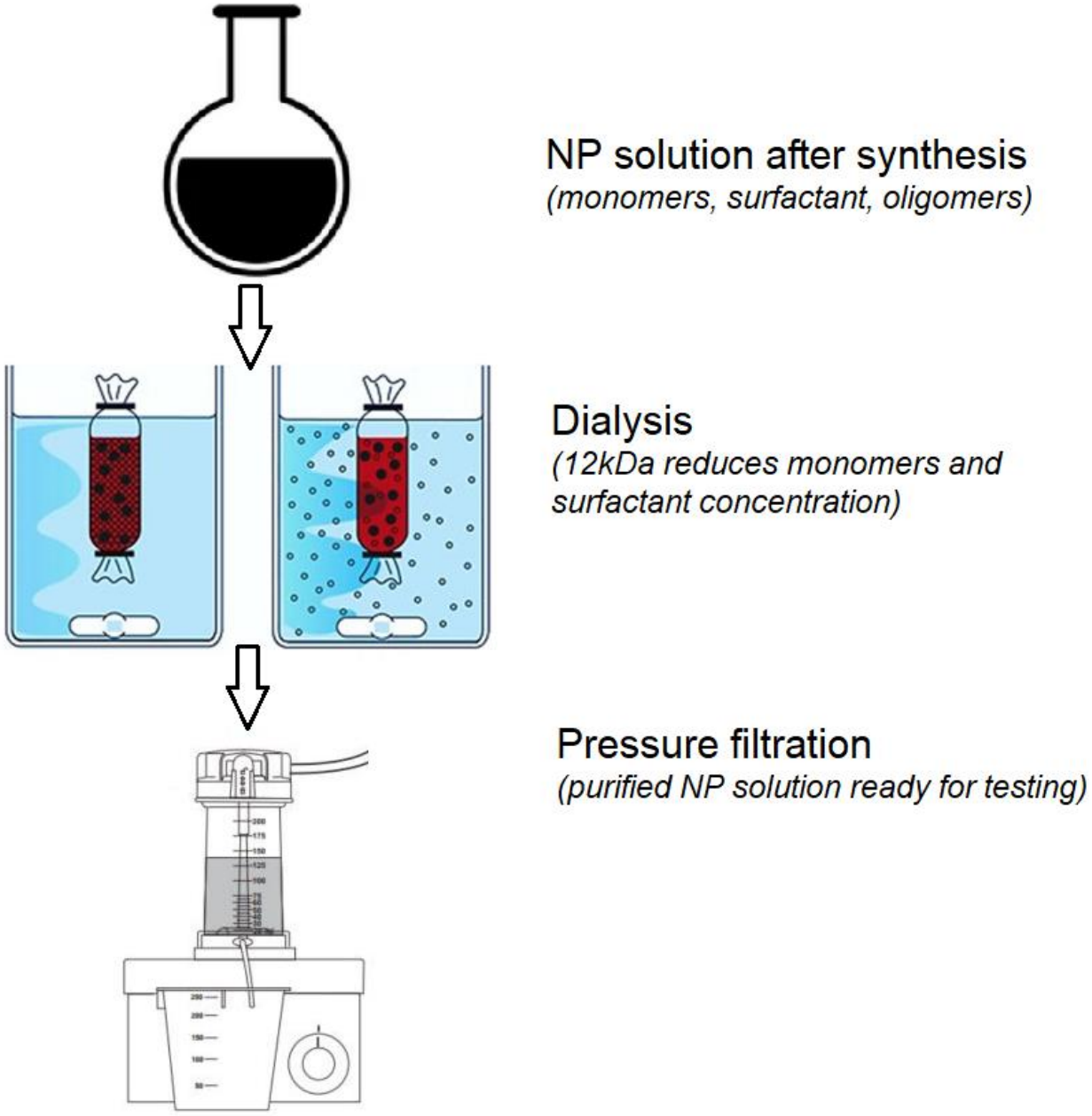

Figure 16: Schematic representation of the purification sequence

3.2.2 Nanoparticles characterization

The aim of this section is to study the link between the synthetic procedure and the resulting diameter, PDI, ζ -potential and TAR residues present on the surface (SurfaceTAR) of the NPs. The goal was to establish if those properties can be fine-tuned through variation in the reagent ratios and use of CTAB.

Table 3: Synthesis information and DLS data for all synthesized NPs. Standard deviation (SD) is shown in brackets for the DLS data.

NP name	DSDMA (%wt)	MMA (%wt)	TAR (%wt)	Surface-TAR (%wt)	Yield (%)	Size (nm)	PDI	ζ-potential
RefMMa	0,00	74,71	23,17	17,13	52	126,96 (1,97)	0,101(0,024)	72,50(3,81)
MASS210	40,36	36,13	21,85	22,46	81	117,73 (1,8)	0,217(0,024)	71,36(1,34)
SS450	78,76	0,00	21,17	13,69	16	149,15 (2,79)	0,214(0,011)	65,36 (4,57)
MASS100	19,21	57,61	20,97	8,13	49	123,19(1,03)	0,180(0,009)	58,60(4,85
SS114	45,78	0,00	22,97	12,54	44	113,84(9,39)	0,334(0,058)	61,43(3,76)
CTABSS1	80,32	0,00	4,19	0,00	-	**Agglomerated**		26,82(7,00)
CTABSS2	80,34	0,00	4,33	0,00	-			-50,15
SS114NR	46,72	0,00	21,97	17,41	48	80,6 (29,91)	0,303(0,107)	54,98(1,93)
CTABMA	0,00	91,61	4,19	3,50	40	95,29(2,43)	0,098(0,016)	29,93(1,06)
CTABSS3	45,97	0,00	22,77	17,66	60	49,99(5,10)	0,244 (0,55)	58,56(2,54)

The naming principle for the NPs follows their composition – MMA-copolymerized NPs contain the prefix MA in their name, while DSDMA-only NPs – do not. The number after the SS (derived from the disulfide bond) indicated the amount of DSDMA in mg used for their synthesis. The total amount of MMA and DSDMA copolymers was maintained constant (~450mg), regardless of their ratio, alongside the amount of TAR (~110mg), thus the naming convention reveals the full synthesis composition of the NP. SS114 and SS114NR – correspond to the same starting material ratio (114mg DSDMA, ~110mg TAR, no MMA), however, SS114 is further loaded with Nile Red dye (NR). NPs synthesized through the CTAB-assisted process do not follow the same naming principle, as they were not considered of interest during the study (see below). CTABMA denotes the MMA-only NPs, synthesized through the CTAB-assisted method, which were used as a non-degradable reference for several experiments.

The synthesized NPs were analyzed through DLS for their hydrodynamic diameter and polydispersity, for their ζ-potential to establish their charge, through TGA to indirectly evaluate their chemical composition and through Ag titration to quantify the number of Br- ions, pertaining to TAR and establish the amount of TAR available at the NP surface.

A reference MMA-based NP sample (RefMMa) was first synthesized through the emulsion polymerization method employing amount/ratios optimized during previous studies. The produced NPs had a diameter of 128,96 nm, a polydispersity index (PDI) of 0,101, a strongly positive ζ-potential (72,5) and surface TAR at 17,13 %wt. The yield of the synthesis, after dialysis and purification was 52%. Those values were used as a benchmark for the consequently synthesized DSDMA-based NPs. The amount of TAR employed in the synthesis was kept constant (+/- 2%wt and 2 mmol), therefore the difference in results (d, PDI, ζ-potential, SurfaceTAR) should be caused only using varying amount of DSDMA, affecting the DSDMA/MMA and the DSDMA/TAR ratios.

Introducing 19,21 %wt of DSDMA to the MMA-based synthesis produced NPs with similar diameter (123,19nm), but increased PDI (0,18). The SurfaceTAR and the ζ-potential were notably decreased, without affecting the NP stability in solution and the synthesis yield was near the reference at 49%. Further increasing the DSDMA amount to 40,36 %wt of copolymer, decreased the NP diameter to below reference levels (117,73) and further increased the PDI to 0,217. The ζ-potential was nearly identical to the reference, while SurfaceTAR was increased to 22,46%wt. The yield was also improved to 81%, even though some bulk polymerization residue was still observed during synthesis. This suggests that an almost 1:1 weight ratio (mol ratio) of DSDM/MMA has a considerable effect on the efficiency of the synthesis, without negatively affecting the physical properties of the resulting NPs.

Importantly, DSDMA-only-based NPs showed a considerable increase in diameter (149,15 nm), maintaining a similar PDI to the 1:1 ratio NPs (0,214). The slight decrease in ζ-potential (65,36), corresponding to a moderate decrease in the SurfaceTAR (13,69), compared to the RefMMa reference, did not affect the NP colloidal stability.
Overall, the observed change in diameter is likely due to the crosslinker nature of DSDMA, more likely creating a more rigid NP structure, thus hindering polymer chain folding and affecting the NP size, depending on the crosslinking degree. As expected, this effect was most pronounced when DSDMA was used as the only monomer (SS450) and least prevalent at low crosslinker concentrations (MASS100). Nonetheless, the decrease in size for MASS210 suggests that at a 1:1%wt ratio of MMA/DSDMA a more compact crosslinked polymeric structure is created, which also resulted in an improved yield. Based on this alone, further experiments should be performed on the effect of the MMA/DSDMA ratio on the NP properties. The linear increase in PDI is likely due to the interference of DSDMA in the linear MMA polymerization process and the amplification of the already present variability in the size of growing NP (within the micelles of different size). The introduced crosslinks are likely not fully homogeneously distributed among the growing NPs, having a higher concentration in larger micelles, leading to further crosslinked NPs, in turn further affecting the size difference between NPs from smaller micelles and those from bigger ones. Therefore, at low DSDMA concentrations PDI is affected to a lesser extent yet is still considerably higher than the MMA-only reference. While at the higher DSDMA concentration (DSDMA-only included) the PDI remains constant, albeit at a higher level, since the maximum crosslink density could be reached and further increasing the DSDMA concentration would not have a pronounced structural effect. This should be tested by further varying the MMA/DSDMA ratio and terminating

polymerization at various times to assess the effect that crosslinking has on the resulting diameter and size distribution.
The non-linear effect on the ζ-potential and the SurfaceTAR from the use of DSDMA could also be attributed to the same crosslinking phenomenon that hinders free folding of the NP polymer chains, allowing for less TAR residues to be exposed to the surface. Or, in the case of MASS210, at a specific ratio, allow for more efficient positioning of TAR on the NP surface.

The yield, on the other hand, was significantly reduced (to 16%) when using DSDMA only. Coupled with the observation of considerable bulk polymerization during synthesis, this suggests serious inefficiencies in the emulsification process and the ability of TAR to keep the used amount of DSDMA into micelles.

In an attempt to improve the low yield and increase size of the DSDMA-only NP, e.g. SS450, a lower amount of DSDMA was used (45,78%wt instead of 78,76%wt for SS450) to achieve a higher TAR/DSDMA ration and potentially improve the micelle-integration of DSDMA during polymerization.

The synthesis yield was successfully improved to 44%, close to the reference, while the resulting NPs had the smallest diameter of all synthesized up to that point (113,84) and a considerably higher PDI of 0,334. The SurfaceTAR was slightly lower than that of SS450 (12,54 vs 13,69) with a corresponding small decrease in ζ-potential (65,36 vs 61,43), without any loss of colloidal stability. The decrease in size was expected, considering the overall lower amount of copolymer. While the drastic increase in PDI suggests an uneven distribution of DSDMA among the TAR micelles at a higher crosslinker/surfactant ratio. A high DSDMA concentration heterogeneity in the colloid particles during the polymerization process could explain the high difference in PDI when comparing SS450 and SS114 synthesis systems, which are essentially composed of the same components. Furthermore, the radical initiator concentration was not adjusted for the lower DSDMA amount (3%wt for SS450 and 8%wt for SS114). It likely also contributes to the higher PDI, as higher radical initiator concentrations produce shorter polymer chains and more varied chain lengths, increasing the variability in the NP size distribution.
Nonetheless, further experiments with DSDMA/TAR ratios and initiator concentrations should provide more conclusive results and allow for more reliable explanations.
Characteristics such as the NP size, stability and surface charge were used as main criteria for assessing the products of consequent synthesis optimizations. The focus was primarily on optimizing the DSDMA - only NPs, as they have the greatest degradation potential.

3.2.3 CTAB-assisted synthesis

After the attempt to improve the DSDMA-only NPs through simply decreasing the amount of precursor, a different synthetic approach was also tested. CTAB was used as a surfactant to reduce the loss of product through agglomeration/bulk polymerization, due to the insolubility of DSDMA and the apparent inefficiency of TAR to fully incorporate it in micelles. TAR was introduced at a lower amount to fulfil its role as a charged copolymer only. It was theorized that

CTAB would possess a higher surfactant power, thus more efficiently integrate DSDMA and the growing polymer chains into micelles, facilitating the emulsion polymerization process and increasing the yield. This approach was demonstrated as effective in a similar PMMA core-shell system by Hoffmann et al., utilizing quaternary ammonium methacrylates similar to TAR as charged copolymers for MMA.

Table 4: Synthesis information and DLS properties for the CTAB-assisted NPs

NP name	%wt DSDMA	%wt MMA	%wt TAR	%wt sTAR	Yield %	Size (SD)	PDI (SD)	ζ-potential (SD)
CTABMA	0	91,61	4,19	3,50	40	95,29(2,43)	0,098(0,016)	29,93(1,06)
CTABSS1	80,32	0,00	4,19	0,00	-	**Agglomerated**		26,82(7,00)
CTABSS2	80,34	0,00	4,33	0,00	-			-50,15
CTABSS3	45,97	0,00	22,77	17,66	60	49,99(5,10)	0,244 (0,55)	58,56(2,54)

The modified procedure was first tested on a PMMA-only NP to serve as a reference. It successfully afforded NPs in a relatively higher yield (40% vs 16%), with a small diameter (95,29nm) and a low PDI (0,098) and with a positive ζ-potential (29,93). It is important to note, the CTABMA ζ-potential and SurfaceTAR were much lower than those of the Nu-21 reference, however, it still showed sufficient colloidal stability.

The DSDMA NPs employing the same recipe, on the other hand, agglomerated during synthesis and had low or non-positive ζ-potential after sonication and immediately started agglomerating thereafter. Applying ultrasound to the starting material solution (CTABSS2) right before the reaction (addition of AIBA) did not yield different results as the produced NPs also agglomerated and did not show a positive charge (ζ-potential). The especially peculiar negative ζ-potential measurements for CTABSS2 are likely due to instrumental error or interference as the non-purified synthesis solution was directly used for measurements. Nonetheless, the persistent agglomeration of the NPs should be the definitive indication of their low/neutral surface charge and the effectiveness of the CTAB synthetic approach.

Consequently, the amount of TAR used alongside the CTAB surfactant was increased to the levels of the initial synthesis approach (~110mg). At this point, the synthesis was performed predominantly to gain insight into the emulsion polymerization process, rather than to improve the resulting NPs. The resulting NPs (CTABSS3) did not agglomerate, had a high positive ζ-potential (58,56) and showed a considerable amount of TAR residues on the surface (17,66 %wt), similar to the properties of the NPs from the non-CTAB assisted synthesis. The high amount of TAR probably allowed for a sufficient amount of charged copolymer to be polymerized into the DSDMA chains. With that, sufficient TAR residues resulted on the surface, imparting a positive charge, and preventing agglomeration. The CTABSS3 average diameter was considerably smaller than all previously synthesized NPs (49,99nm). While the PDI showed some improvement towards lower values, compared to SS114 (0,244 vs. 0,344), it was still higher than that of all other DSDMA-containing NPs. However, upon further investigation of the size distribution of CTABSS3, it consisted of 3 different NP populations (see Figure 17). Potentially, the high amount of TAR allowed for the formation of TAR micelles encapsulating DSDMA as well as the CTAB micelles,

containing both TAR and DSDMA, resulting in a heterogeneous mixture of NPs. Ultimately, the use of CTAB in any form did not yield usable NPs and provided limited insight into pathways for optimization of the original synthesis.

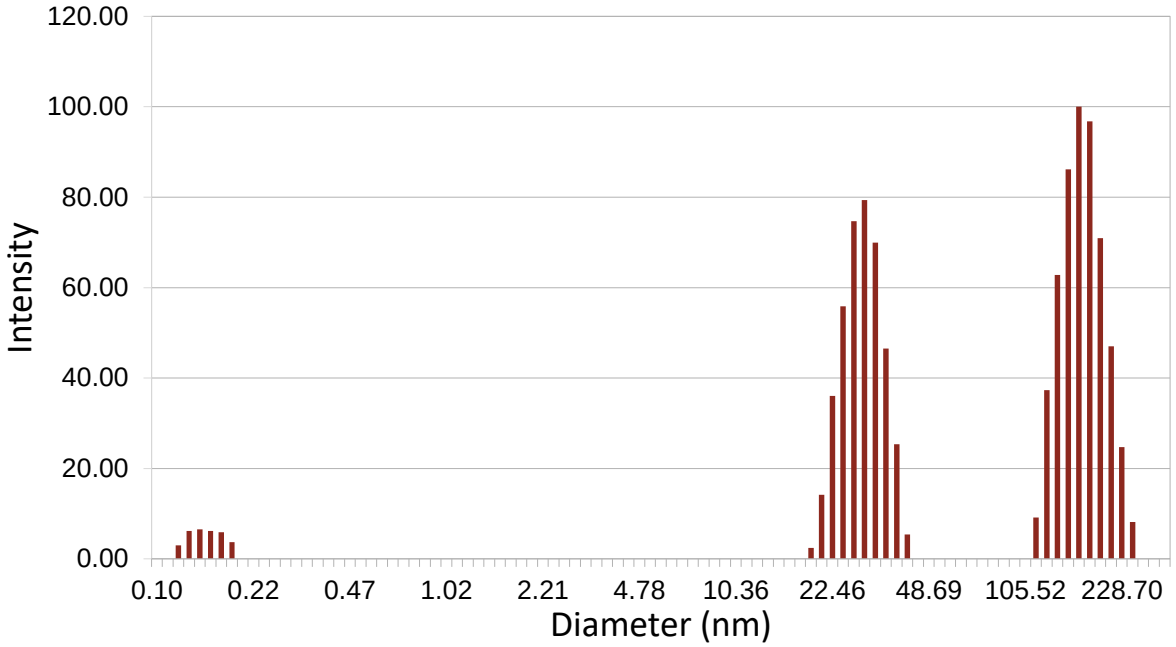

Figure 17: The size distribution of CTABSS3

Overall, four of the synthesized DSDMA NPs were suitable for further tests due to their colloidal stability and singular size distribution. They also possessed sufficiently similar physical properties, diameter and surface charge to the PMMA-only analog, and showed only a moderately higher PDI, still within acceptable values for drug carrier applications (<0.3). The synthesis process was not further optimized for the DSDMA precursor, but several key areas for further research were highlighted. It was demonstrated that a yield of 81% could be practically achieved, even with TAR acting as both a surfactant and a copolymer and with rigorous purification procedures.

However, the employed identification techniques (DLS, titration) could not provide exhaustive data on the structure and composition of the synthesized NP, nor significant insights into the specific mechanism for NP formation with DSDMA.

3.3 TGA

The aim of the TGA study was to clarify the actual composition of the synthesized NPs, especially concerning their actual (rather than intended) DSDMA content. Also, if the analytical approach proved successful, it would be put forward as a reference tool for further research developments on the subject/NP system.

Despite the relative simplicity of the NP system, both due to its straightforward synthesis and low number of constituents (chemical components), it is unreasonable to assume that the ratio of the starting materials is directly represented in the NPs structure. Considering the low yields (<50%) for most NPs and the formation of bulk residue, it was critical to establish the actual composition of the NPs, and to establish whether it follows the DSDMA/MMA ratio of the starting materials. Having accurate knowledge on the actual NP composition that can then be related to the results from their functionality studies is crucial for successfully building a **structure-function relationship**, which, in turn, is a key approach to biomaterial research and drug delivery systems.

TGA was chosen as the main technique for the composition analysis. It requires minimal sample preparation and offers relatively high speed and a low cost of analysis. It is well suited for the initial evaluation and comparisons of a larger number of samples during the ongoing synthesis optimization. Most importantly, it is suitable for a direct comparison between the bulk polymer residue, the NPs agglomerates and the charged NPs from solution, which would be much more difficult with other available techniques.

Nonetheless, TGA does not give direct information on the structures within the NPs. Still, with a suitable reference and background information, it can provide insight into the structure of a polymeric material. TGA shows the thermal scission of bonds and consequent loss of volatile fragments from the compound, measuring the resulting weight lost from the sample. When performed in an inert atmosphere, like in the present study, no oxidation takes place and only the loss through fragments and through intra-compound reactions is responsible for the observed weight loss. If the components within the NP structure have sufficiently different decomposition temperatures, the measured weight loss curve should provide qualitative and semi-quantitative information on the NP composition. When that is the case, as in the present study, identifying which peak corresponds to which compound and/or structure is the main analytical challenge. However, the availability of suitable reference materials can facilitate the analysis.

Additionally, the thermal decomposition profile of a multicomponent NP should not greatly differ from that of the single-component NPs, synthesized from the same compounds separately, and having samples with different ratios of these components could further help the peak identification process, and this was the case of the present study. The reference was provided by the TGA curves of TAR, PMMA-only charged NPs (CTABMA) and DSDMA - only charged NPs (SS450 and SS114). Ag titration provides a separate point of reference as a method for the characterization of the chemical composition of the NPs surface. Additional background

information was provided by the synthesis procedures - the exact amount/ratio of the limited number of starting materials (TAR, DSDMA, MMA).

TGA has another benefit to the specific NP system of interest, since it can provide insight on the structure/morphology of a polymeric material, such as crosslinking, and it can highlight the structural differences between the synthesized NPs and their respective bulk residue. This is mostly because crosslinked or more dense polymeric systems usually better resist degradation, showing higher degradation temperature than a less crosslinked/dense system from the same material. Furthermore, a difference in decomposition temperature for two samples of the same chemical composition could indicate a significant difference in the surrounding structure/chemical environment of the specific compound/substance.

A stepwise comparison was employed to identify the specific peaks within the derivative of the TGA curve. Peak identification was referenced with literature sources. The NP TGA curves were first referenced to those of TAR, identifying the corresponding TAR peak. Then, the NP TGA curves were referenced to those of CTABMA (TAR and PMMA), confirming the TAR-related peak and identifying peaks corresponding to the PMMA structure. Finally, the NP TGA curves were referenced to those of SS450 and SS114 (TAR and DSDMA), identifying the corresponding DSDMA-related peak and adjusting the assignment of the PMMA peaks, as an effect of the presence of DSDMA. Consequently, the peak onset, duration and shape was observed and compared among all measured samples.

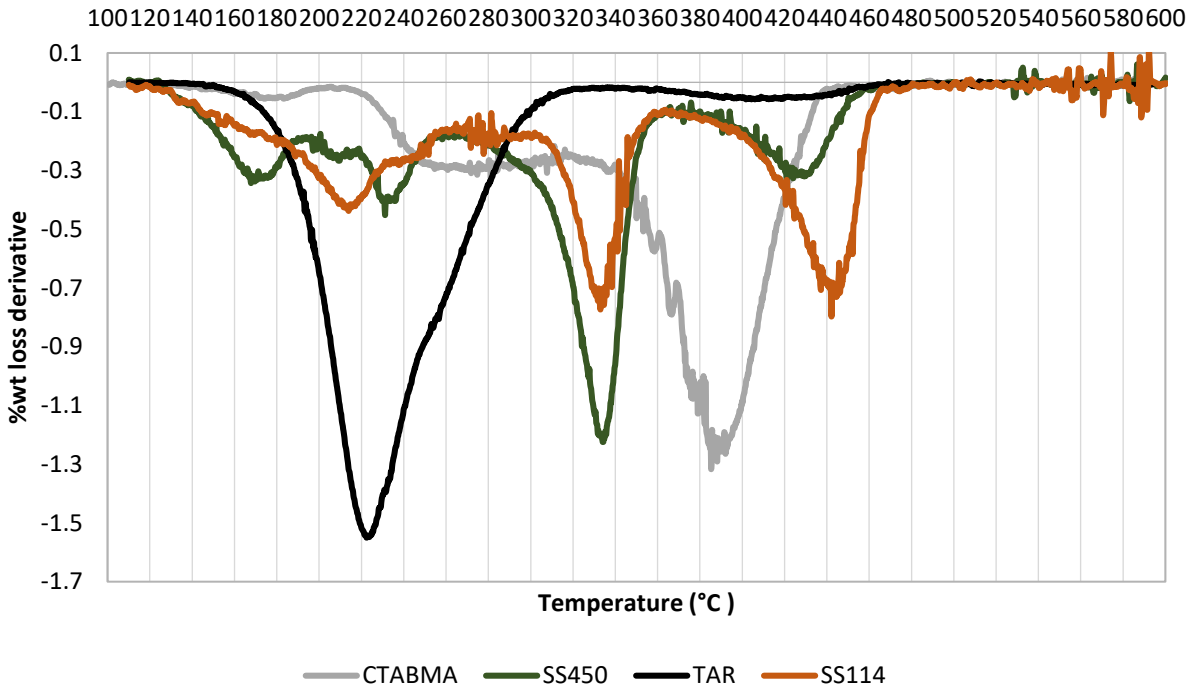

Figure 18: Direct comparison of some of the differential TGA curves used for the peak assignment.

The discrepancies (10-20 °C) in the onset of the peaks from the NPs and peaks from the respective standalone components (TAR, CTABMA) are likely not significant as there should be considerable difference in the sample weight and packing, which affect heat conductivity and distribution. The weight loss curve represents bond cleavage, which is caused by the sufficient (thermal) energy available to break the specific bond. The weight loss, however, is correlated to temperature (x axis) and not availability of (thermal) energy. Temperature is a statistical (average) representation of available thermal energy. Therefore, a broader peak shape, rather than a sharp plateau is expected. Some variation in the values is always present across analysis runs and especially for heterogeneous samples. Furthermore, as the ramp of temperature is quite high (10 °C/min), a difference of 10-20 °C could be fully attributed to differences in heat conductivity and/or specific structural differences (degree of crosslinking, density of the polymer, MW of the polymer), rather than fundamental differences in the chemical nature of the structures.
The placement of the tip of the peak is related more to the overall amount of decomposing compound, rather than its nature and composition. Finally, the end of the peak is solely related to the amount of compound - more material takes longer to decompose, despite the increasing temperature.

Despite the indirect structural information from TGA, it should be reasonable to directly compare the weight loss data of different NP formulations, derived from TGA curves, and correlate those findings to the titration data as methods have a gravimetric component (weight loss for TGA and moles TAR per gram of NPs for the Ag titration).

3.3.1 Differential curve peak assignment

After the comparison of the differential weight loss curves of all synthesized NPs, the peaks were assigned in the following manner (**Assigned peak name** (onset temp. - end temperature):

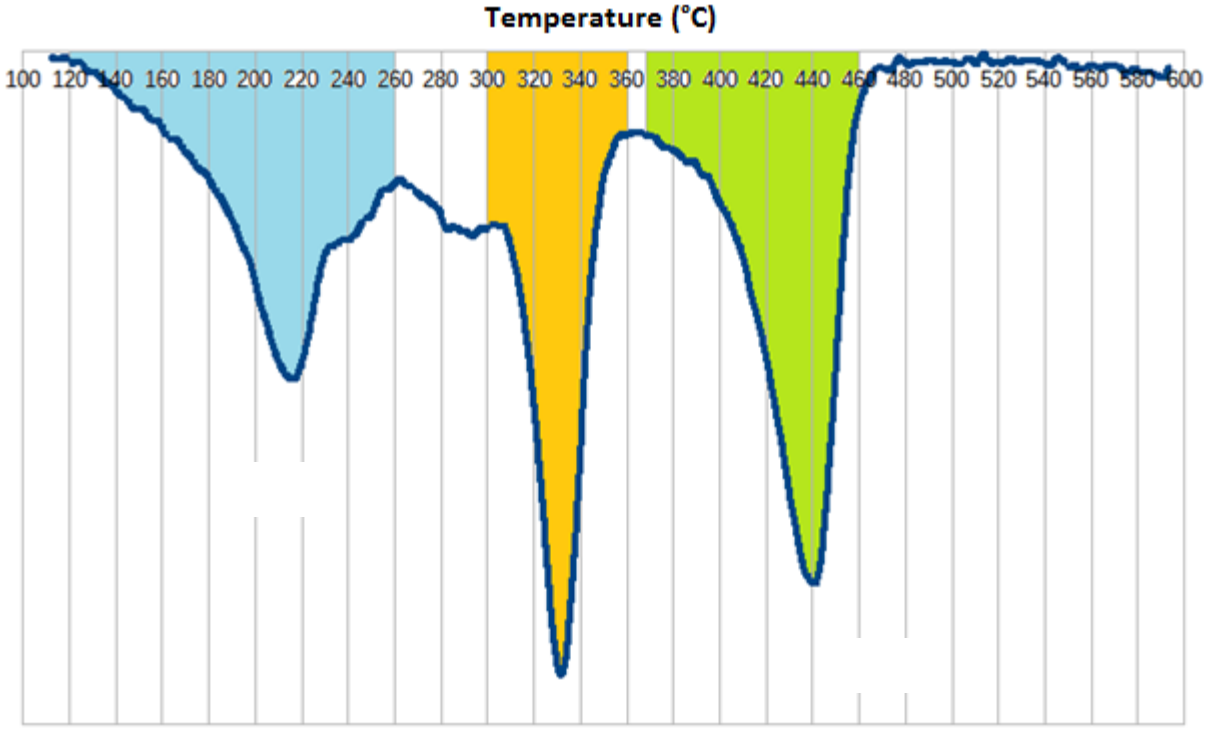

Figure 19: The TGA derivative curve of CTABSS3 with the TAR peak highlighted in blue, the DSDMA peak – in yellow and the MMA peak in green. The MA plateau is seen between the TAR peak and the DSDMA peak (not highlighted).

The **TAR peak** (120-240 °CC) was confirmed by the TAR reference, the CTABMA reference and from literature sources for the decomposition of quaternary ammonium surfactants. It should not represent the full weight of the total amount of TAR incorporated in the NP, as only a part of the TAR molecule decomposes (MA remains). This is supported by the higher amount of TAR found on the surface of the NP through Ag titration than from TGA peak itself. The ratio of TAR on the surface (expressed as %wt) and the TAR peak shows the relative proportion of TAR molecules on the surface vs. total. MASS210 and SS450 show higher TAR% on the surface (from titration) than from the TAR peak, which is expected as the TAR peak does not represent the full TAR molecular structure (in the polymer). However, all other NPs show a larger proportion of the TAR peak (Figure 22), even though a lower one is expected, suggesting that there is a considerable amount of TAR residues in the bulk.

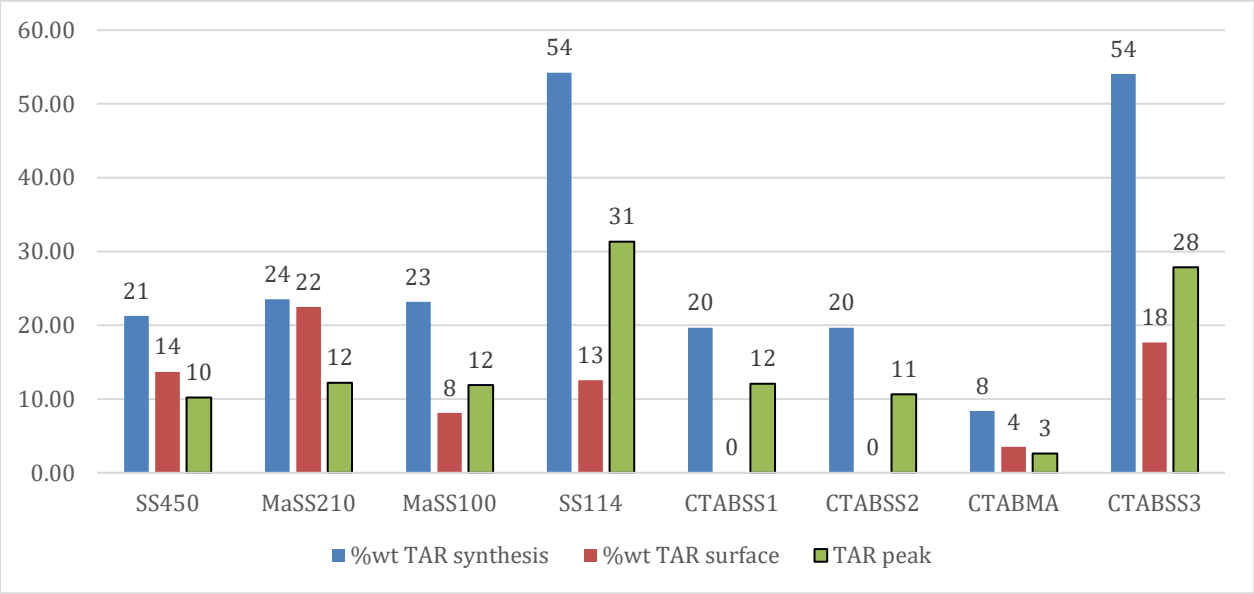

Figure 20: Comparison of TAR-related values for all synthesized NPs. %wtTAR synthesis – percentage of TAR expected from the amount used in the synthesis, %wtTAR surface – percentage of TAR present on the surfaced of the NPs, found through Ag titration

The post TAR region (~220 °C-310) is characterized either with a moderate peak for the SS450 NPs, or with a stable plateau of weight loss, which is observed to some extent in all other samples. The plateau is most prominent in CTABMA (reference) and more pronounced in MMA-containing NPs (Table 5, last column). Nonetheless, it can be seen in all measurements and cannot be attributed to a specific decomposition fragment with the used identification approach. Furthermore, it is likely related to a certain polymeric structure, not a singular compound, as it is present in all NPs, but is not present in the residues, neither in agglomerated NPs. Likely the specific structure the peak represents is not formed during bulk polymerization and is lost during the agglomeration process of non-charged NPs. As it cannot be accurately/reliably assigned to a specific compound or structure, the weight loss from this region was not considered in the final data analysis. Further tests with higher sensitivity will be performed using TGA results as cross-references to other analytic techniques.

Table 5: Synthesis parameters and properties of the NPs compared to their MA plateau.

NP name	DSDMA Weight %	TAR weight%	MMA Weight %	%MA plateau
MaSS210	40,36	23,51	36,13	**16,82**
SS450	78,76	21,24	0,00	**18,29**
MaSS100	19,21	23,18	57,61	**13,34**
SS114	45,78	54,22	0,00	**6,75**
CTABSS1	80,32	19,68	0,00	**0,00**
CTABSS2	80,34	19,66	0,00	**0,00**
CTABMA	0,00	8,39	91,61	**24,51**
CTABSS3	45,97	54,03	0,00	**9,19**

The **DSDMA peak (280/300-360)** always appears as a sharp peak, especially in residues and aggregated NPs. As expected, it is most pronounced in DSDMA-only based NPs (SS450, CTABSS1, CTABSS2), while being absent in the CTABMA curve. It most likely represents the decomposition of the crosslinks and de-esterification of the DSDMA residues, separating from the methacrylic backbone. The peak shows lower than expected relative prevalence for SS114 and MASS210. It is the most prevalent peak within the curves of all residues, even MASS210, thus indicating that DSDMA is concentrated in the bulk residue during synthesis, rather than evenly represented in all resulting polymeric products. In turn, this would suggest that the DSDMA/MMA - copolymer NPs contain less DSDMA than originally intended. This is further supported by the similarity in the relative abundance of DSDMA (by TGA peak area) between MASS100, MASS210 and SS114. From the ratios of starting materials, it is expected that SS114 would have the highest DSDMA %wt, closely followed by MASS210. MASS100 should contain half the amount of DSDMA of MASS210 and SS114. However, from the TGA analysis it is shown that all three NPs contain similar amounts of DSDMA, represented by the relative size of their DSDMA peaks (Table 6, entry 1-3). The lower DSDMA peak in SS114 could be attributed to the higher prevalence of the TAR peak and the higher TAR/DSDMA ratio of the starting products (Table 6, entry 4). As for MASS210, with the residues containing a disproportionate amount of DSDMA (3,73 times more than the NP itself; Table 7, ratios highlighted in red), it is reasonable to assume that MASS210 has a lower DSDMA content than originally intended in the synthesis. As no bulk residue was produced for MASS100, similar conclusions cannot be made. The composition of MASS100 in respect to DSDMA could be further clarified through its final residue amount (see Final residue section), degradation behavior (see DTT degradation section) and ROS activity (see ROS testing section).

Table 6: Synthesis parameters and properties of the NPs compared to their DSDMA peak

NP name	DSDMA Weight %	MMA Weight %	TAR weight%	%DSDMA peak
MaSS210	40,36	36,13	23,51	**21,43**
SS450	78,76	0,00	21,24	**47,1**
MaSS100	19,21	57,61	23,18	**25,6**
SS114	45,78	0,00	54,22	**23,16**
CTABSS1	80,32	0,00	19,68	**48,08**
CTABSS2	80,34	0,00	19,66	**53,68**
CTABMA	0,00	91,61	8,39	**0,00**
CTABSS3	45,97	0,00	54,03	**32,84**

Table 7: Synthesis parameters and properties of the bulk NP residues and their comparative TGA peak ratios to the respective synthesized NPs.

Sample name	DSDMA Weight %	MMA Weight %	TAR peak	%DSDMA peak	% MA peak	DSDMA peak ratio to NP	MA peak ratio to NP
MaSS210residue	40,36	36,13	0,95	**79,92**	11,14	**3,73**	**0,23**
SS450residue	78,76	0,00	6,50	**84,84**	7,84	**1,8**	**0,53**

The MA peak (last peak in all curves - 380 to 480 °C) corresponds to the final degradation of the methacrylic chain. It is most prevalent in CTABMA (72,73%). It is least prevalent in the DSDMA-only NPs (lowest in SS450 - 14,76%; Table 8, entry 2). Data from the bulk residues shows they have an even lower MA peak (<12%), than the actual nanoparticles. The comparison between the MA peak of the NPs and the MA peak of the bulk (MA peak ratio) shows a disproportionate accumulation of MMA withing the NPs, similarly to that of DSDMA within the bulk residue (Table 7, ratios highlighted in red for DSDMA and blue for MA). This further suggests the presence of "copolymer discrimination" during the polymerization process, in favor of MMA incorporating preferentially within the NPs.

Table 8: Synthesis parameters and properties of the NPs compared to their MA peak

NP name	DSDMA Weight %	MMA Weight %	TAR weight%	%DSDMA peak	% MA peak
MaSS210	40,36	36,13	23,50	21,43	**48**
SS450	78,76	0,00	21,24	47,1	**14,76**
MaSS100	19,21	57,61	23,18	25,6	**49,05**
SS114	45,78	0,00	54,22	23,16	**31,59**
CTABSS1	80,32	0,00	19,68	48,08	**29,46**
CTABSS2	80,34	0,00	19,66	53,68	**27,76**
CTABMA	0,00	91,61	8,39	0	**72,73**
CTABSS3	45,97	0,00	54,03	32,84	**31,73**

3.3.2 Final residue analysis

Titration and the TAR peak provide an exhaustive insight into the presence of TAR within the NPs (both on the surface and within the core). However, there are inconsistencies in the analysis of DSDMA-fragments, which are crucial to the degradability of the studied system. Relying on degradation tests and other property tests (indirect) to gain insight into the SS-related composition is cumbersome and unreliable, so another attempt was made to establish a method for finding the DSDMA amount within the NPs.
The amount of residual material after the decomposition of the main components of the NPs was used to gauge the amount of TAR and DSDMA present in the NPs as both contain components that are not volatilized under inert atmosphere at the degradation temperatures for the methacrylate structures, namely the bromide ion from TAR and the sulfur from DSDMA.

More residual weight after 480°C was expected to correspond to more DSDMA and TAR within the NP structure. Then, the DSDMA peak from the TGA curve can be correlated to the residual amount to evaluate its accuracy in representing the DSDMA components in the structure and to potentially highlight and rectify any inconsistencies in the previous peak identification and analysis, especially for the MASS100 NP.

Only data from the non-agglomerated NPs were used as those are the ones of interest to specifically identify how much DSDMA there is in their structure. Furthermore, the agglomeration might have affected the representativeness of the attributed peaks (aka PMMA decomposes within the DSDMA peak and vice-versa) making the bulk residue data unsuitable for an accurate analysis.

The test was performed through evaluation of the correlation coefficient (R^2) between pairs of values for all the NPs of interest. The pairs always included the final TGA residue and one of the following parameters: the DSDMA amount used for the synthesis, the DSDMA peak, the TAR peak. Correlation coefficient scores below 0,40 were considered as weak correlation, below 0,7 – as moderate correlation, below 0,9 – as strong correlation and above 0,9 – excellent correlation, as per conventional interpretation throughout literature. (Schober et al., 2018)

The correlation between the amount of DSDMA used in the synthesis and the final residue peak (0,755 as seen in Table 9) is used as a baseline, as it should loosely represent the amount of DSDMA within the NPs but should not account for any discrimination in the actual NP composition. A strong, but not excellent correlation is expected for the pair. Conversely, the DSDMA peak correlation to the final residue should strongly correlate to the actual DSDMA amount in the NPs, if the DSDMA peak is truly representative of the DSDMA-residue within the structure. Low correlation coefficient values should point towards inconsistencies either in the peak data or the analysis and interpretation of the results.

Table 8: Correlation of NP characteristics to the amount of final residue of the TGA

NP name	DSDMA%wt	%DSDMA peak	%TAR peak	TAR+DSDMA peak	%Residue TGA
MaSS210	40,36	21,43	10,22	31,65	**3,32**
SS450	78,76	47,10	12,20	59,3	**7,65**
MaSS100	19,21	25,60	11,90	37,5	**0,00**
SS114	45,78	23,16	31,32	54,48	**7,04**
CTABMA	0,00	0	2,62	2,62	**0,00**
CTABSS3	45,97	32,84	27,86	60,70	**7,47**
R^2	**0,755**	**0,515**	**0,528**	**0,741**	**1**

As seen in Table 8, there was a strong correlation between the DSDMA amount added in the synthesis and the %wt of final residue (R^2=0,755), as expected. Similarly, analyzing the TGA data, there was good correlation for the sum of peaks for the residue-producing components TAR and DSDMA (R^2=0,741). The sum of the two peaks should have a higher correlation to the final residue, than their separate values, as seen in the results, since both compounds contribute to the final residue independently of each other. Nonetheless, the correlation coefficient was lower than expected, suggesting some inconsistencies in the date or the approach.

Table 9: Correlation table after removal of MaSS100 data due to suspected errors

NP name	DSDMA%wt	%DSDMA peak	%TAR peak	TAR+DSDMA peak	%Residue TGA
MaSS210	40,36	21,43	10,22	31,65	3,32
SS450	78,76	47,1	12,20	59,3	7,65
SS114	45,78	23,16	31,32	54,48	7,04
CTABMA	0,00	0	2,62	2,62	0
CTABSS3	45,97	32,84	27,86	60,7	7,47
R^2	**0,757**	**0,785**	**0,595**	**0,993**	**1**

Interestingly, removing MASS100 data from the analysis greatly improves the correlation for the questionable data pair (to better-than-expected strong correlation levels), and marginally improves the correlation for all other comparisons (Table 9, last entry). Thus, indicating that the MASS100 measurements might have deviations, likely – the DSDMA peak is not fully representative of the DSDMA amount, likely due to interference from the large MA peak or potential misprocessing of the data. No such positive effect on the correlation was observed with the removal of any other NPs, while MASS100 remained in the comparison.

MASS100 showed no final residue which is consistent only with non-DSDMA containing NPs. Therefore, it is likely that very little (below TGA detection limit) DSMDA is present within the MASS100 NPs and certainly less than the amount intended in the synthesis. The DTT degradation tests and ROS studies served as further evidence (see below). It is possible that DSDMA was lost through the same processes as with MASS210 – bulk polymerization and

discrimination by PMMA, however, due to the small amount of bulk residue it was not visible in the synthesis solution and was not detected.
Overall, the results indicated that using a TGA peak method for gauging DSDMA content is equally as effective and potentially superior to relying on the DSDMA synthesis concentrations. Furthermore, the final residue data can be used to check for any processing and interpretation errors in the TGA.

To further evaluate the NPs' composition, it was first important to establish if there was any copolymer-bias during the synthesis of NPs, and this was tested through the TGA analysis of the synthesized NP and their bulk polymerization residue. It was found that the emulsion polymerization process favored a higher MMA content in the actual NPs and the precursor remained predominantly in the agglomerate. Nonetheless, DSDMA was part of the structure of all NPs, albeit at lower levels than expected for the MMA-copolymerized NPs. All NPs, apart from MASS210 likely contained a considerable amount of TAR residues also within their core, apart from their surface. MASS210 likely contained less DSDMA than initially planned, compensated by a higher MMA content. MASS100 likely contains minimal amounts of DSDMA, closely resembling a PMMA-only NPs. With the NP composition more clearly established, the properties tests can further clarify any inconsistencies related to relative amounts of their constituents and most importantly – a more accurate structure-function relationship can be made for the system.

3.3.3 Future improvement for composition analysis

A more reliable and precise approach to analyzing the composition of the NPs would be through a sulfur analyzer. The amount of S should be directly proportional to the amount of DSDMA within the NPs. It should also directly indicate the potential number of cleavable disulfide links within the NP.

To precisely establish the total amount of TAR within the NPs a nitrogen analyzer could be of use. This would also provide more insight into the polymerization mechanism, selectivity and overall NPs structure, allowing for a more accurate quantification of the total number of TAR residues in the NPs.

3.4 DTT degradation experiments

The scope of this experiments was to establish if the NPs degrade under reducing conditions, and to theorize the mode of degradation, while establishing a link between the morphology and composition (see previous paragraph) and the degradation behavior of the NPs.

After firmly establishing that the precursor was in fact present within the bulk of the NPs, its degradability was evaluated, alongside the overall NP integrity/behavior when exposed to a reducing environment.

In previous research, the degradation ability and rate of disulfide-containing NPs/materials has often been evaluated with DTT. It serves as a more practical in-vitro substitute to GSH, when not working with cell cultures. The effect of DTT on the morphology and composition of the NPs can be monitored through various techniques. The technique of choice for our study was DLS, as it gives information on the overall diameter and size distribution of the NPs. Degradation is usually evident through a drastic change in diameter (decrease) or changes in the size distribution and polydispersity of the NP sample (polydispersity increases and populations of different sizes - usually smaller than the initial one). However, depending on the specific NP material several other degradations behavior can be observed. The visible appearance of agglomerates or the disappearance of any NPs (observed through DLS) are definitive signs for degradation. However, depending on the experimental design, especially the window of observation and data collection, complete degradation might not be observed, even though the material is fully degradable. The concentration of DTT (~9mM) was chosen to be similar to that generally described in literature - 5-15 mM (Sun et al., 2013; Sun et al., 2018; Wu et al., 2015), being representative of the tumor environment. The timepoints for sampling were arbitrarily chosen as the degradation profile of the NPs was completely unknown.

DTT degradation is known to occur after ~3 days and accelerate considerably after 5 days at rt. Therefore, the endpoint to any DTT-induced degradation could fall within the 7 days observation window. As a result, if full degradation and loss of signal is not observed after day 7, the degradation processes can still be detected through carefully investigating the d, PDI and overall distribution.

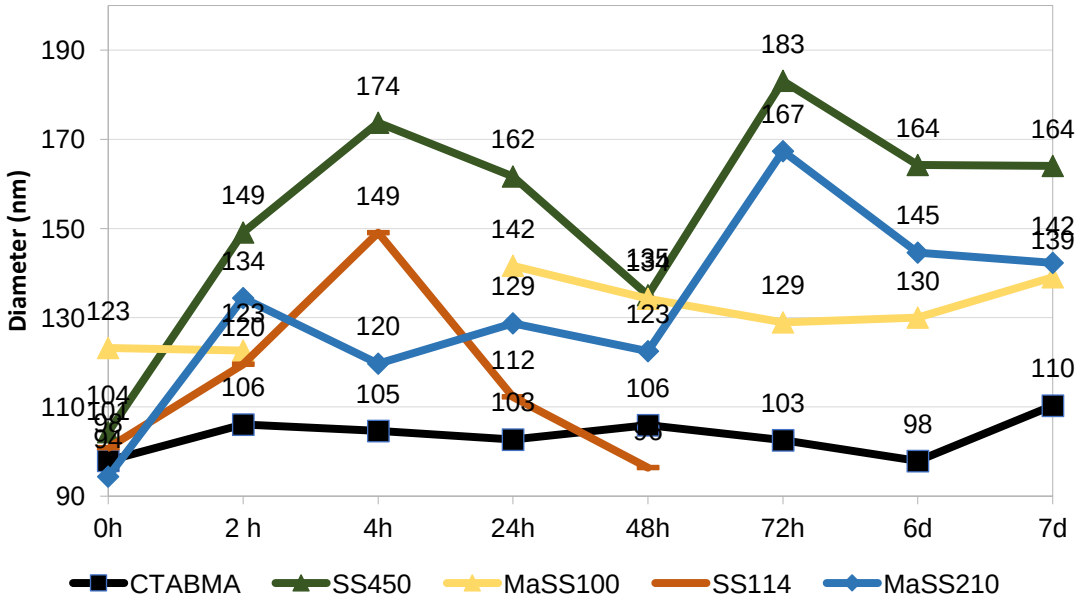

Figure 21: Diameter change over time during the DTT degradation tests

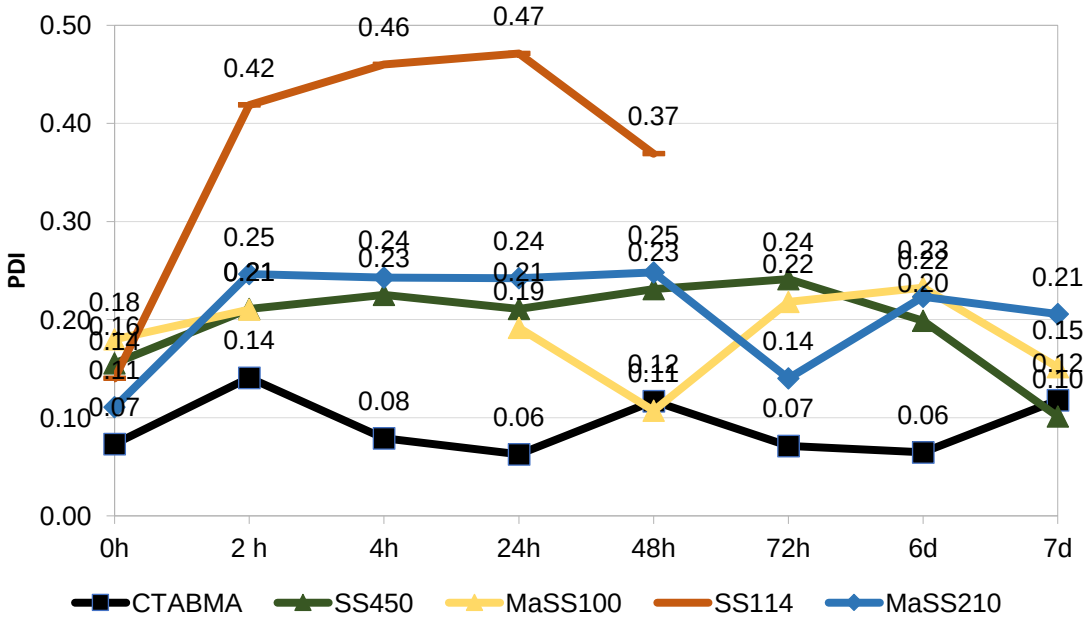

Figure 22: PDI change over time during the DTT degradation tests

As expected, CTABMA diameter and PDI remained relatively constant. No notable changes in the size distribution were observed (Figure 21 and Figure 22, black line).

SS114 decomposed completely, with a sharp increase in PDI already after 2h of DTT exposure and complete loss of signal at 72h after the start of the test (Figure 22, orange line). The sharp increase in diameter consequently decreases after 4h, coupled with the considerable increase in PDI suggest significant swelling of the NP, most likely as a result of crosslink cleavage. Interestingly, the PDI of SS114 upon introduction of DTT (0,140) was considerably lower than after the purification procedure (0,334). This could indicate that DTT had an immediate effect on the size distribution of the SS114, likely completely decomposing the smallest/least crosslinked species. Such an assumption is not unreasonable as a considerable effect on size and PDI could be observed for most NPs as early as 2h after the start of the test.

Similar swelling behavior was observed for the SS450 (Figure 21&22, green line) and, to a lesser extent, MASS210 NPs (Figure 21&22, blue line). SS450 showed an even higher increase in diameter than SS114 after 4h, but only a moderate increase in PDI, while MASS210 fared in-between. Most notably, MASS210 and SS450 showed a decrease in diameter, before a consequent swelling at 72h after the initial peak at 4h. This is likely due to the sequence of erosion and swelling as a result of disulfide cleavage.

Initially, the internal crosslinks are cleaved under reducing conditions allowing for a less hindered chain folding, which results in the swelling of the NP. Consequently, fragments from the swollen NP are cleaved, as they are more exposed to the reducing environment and the diameter is reduced. In turn, more internal crosslinks are exposed and cleaved, and further swelling is observed with an even higher increase in diameter, as the polymer chains in the cores can be

positioned even more freely. MASS100 showed the most modest variations in both diameter and PDI, with PDI returning to initial values at the end of the test (Figure 21&22, yellow line). This behavior was expected, as MASS100 contained the least amount of degradable DSDMA copolymer by design (19,21 %wt) and was suspected to actually contain only trace amounts after the analysis of TGA results, chiefly the lack of final decomposition residue. Missing data points prevent the observation of a peak in diameter at 4h, as in the other NPs. However, the lack of change in diameter at 72h, in contrast to SS450 and MASS210, suggests that MASS100 contained an insufficient amount of DSDMA for significant degradation. Only SS114 fully degraded during the timespan of the test, most likely due to its smaller size, lower amount of DSDMA and presence of considerable amounts of TAR within the structure. Using less DSDMA during synthesis, whilst achieving a similar size to the 4x more DSDMA NPs most likely indicates a less crosslinked (more linear), less dense structure, which in turn should be faster to degrade due to SS cleavage. Furthermore, the high prevalence of charged TAR residues within the bulk of the NP potentially accelerated its degradation by decreasing the hydrophobicity of the NP core, which facilitated the permeation of DTT solution and the consequent swelling and erosion of the NP structure

Overall, it was confirmed that the use of DSDMA as a copolymer, effectively imparts biodegradability to the charged core-shell NPs. The mechanism of degradation most likely involves initial swelling and consequent fragmentation and potentially has several iterations before complete decomposition of the NPs is observed. MASS100 was further proven to contain minimal amounts of DSDMA as it behaved similarly to the PMMA-only CTABMA. Nonetheless, to conclusively establish the degradability of the other NP samples (MASS210, SS450, MASS100) further tests must be performed, extending the time of observation. Indeed, for drug delivery purposes a burst NPs degradation with consequent release of the active cargo, is not beneficial, and additional analysis and optimization should be carried out to set out the best-performing NP preparation, at least in vitro, to further explore these systems in cells and animals.

3.4.1 Limitations

The main limitations to the study include the lack of control over DTT decomposition/concentration in the simulation media. DTT thermal decomposition and oxidation from air exposure most likely decreased the initial concentration to some extent throughout the experiment. To control limitations arising by DTT, the test should be performed under an inert atmosphere and with addition of DTT solution after 3 and/or 5 days. Furthermore, the presence of O2 in solution, could facilitate re-oxidation of the thiol groups on the partially degraded NP and result in reforming the disulfide crosslinks, despite being a highly unlikely scenario at the tested concentration of reducing agent. In fact, this process would be a factor only at low DTT concentrations, which would be reached at the later stages of the test, where bulk cleavage of disulfide bonds should have already considerably disrupted the NP (swelling) and prevented facile crosslink regeneration. The test was designed as a material study to prove the effect of the degradable crosslinker.

In an actual tumor environment the reducing agent (GSH) would be constantly replenished through the cell metabolism and the concentration will remain relatively constant throughout the lifetime of the NPs. Evaluation of the degradation rate and the ability to achieve complete degradation should be performed in cells with GSH for the most representative results.

It is important to note that the NPs could not be tested for their stability in non-reducing conditions (PBS etc) as they showed unstable signals in DLS immediately upon introduction to the buffer solution. Most likely this is a result of the negative charge of the buffer (salts) interacting with the positive surface charge of the NPs.

3.5 ROS production studies

Goal - to test if the NPs retain their ability to electrostatically load PS and be used as PS-anchors/drug delivery systems. To further investigate the ROS producing ability of the NPs themselves. To find a link between the ROS producing ability and the composition and morphology of the NPs (see the synthesis paragraph)

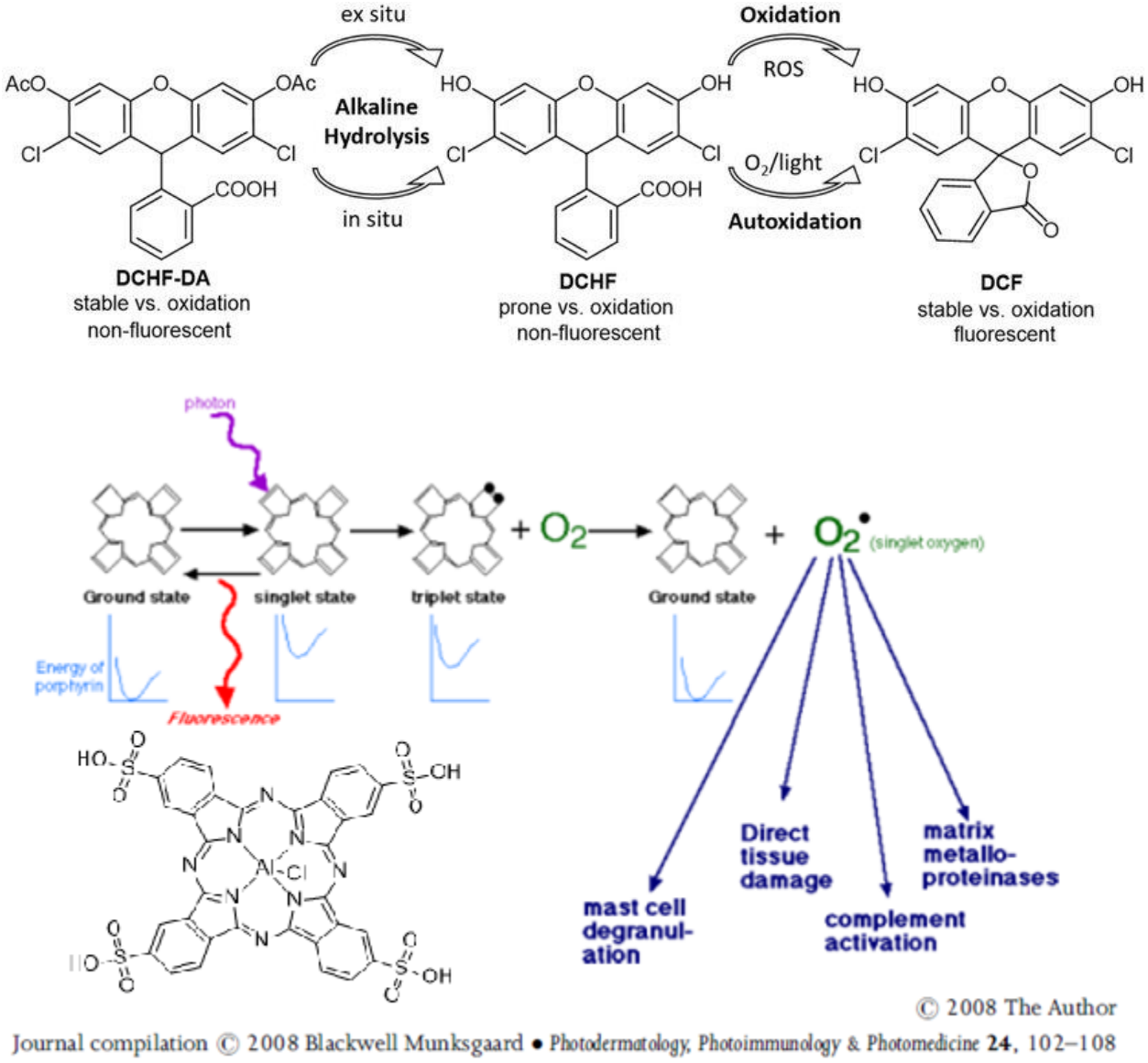

Figure 23: The mechanism of action of the flourecin ROS probe used in the study (top), the structure of Tetrasulfonated Aluminum Phthalocyanine (bottom left corner) and the general mechanism of ROS production of porphyrins (middle reaction scheme).
Note : Adapted from doi:10.1371/journal.pone.0228644

With the degradability and the general chemical composition of the DSDMA NPs confirmed, it was important to establish if the new NP system has retained the useful properties of the original non-degradable analogue. Among those properties is the electrostatic loading of photosensitizers to the positive surface of the NPs, which allows for use in PDT, as described in the Introduction. Tetrasulfonated Aluminum Phthalocyanine (AlPCs4, Figure 23, bottom left) was chosen as a model PS, due to its commercial availability and its successful application in previously studied systems. It was loaded onto the NPs through a simple and well-proven method involving solubilization in water and vortexing with the NPs. To confirm that all of the PS was, in fact, loaded onto the NPs, the NP/PS solution was centrifuged through a 100KDa filter and both the permeate and the filtrate (resuspended in H_2O, red curve in Figure 24) were analyzed through UV-Vis spectroscopy. No PS-related peaks were observed in the permeate (Blue curve in Figure 24), which was considered sufficient evidence that all PS was electrostatically attached/coordinated onto the NP surface.

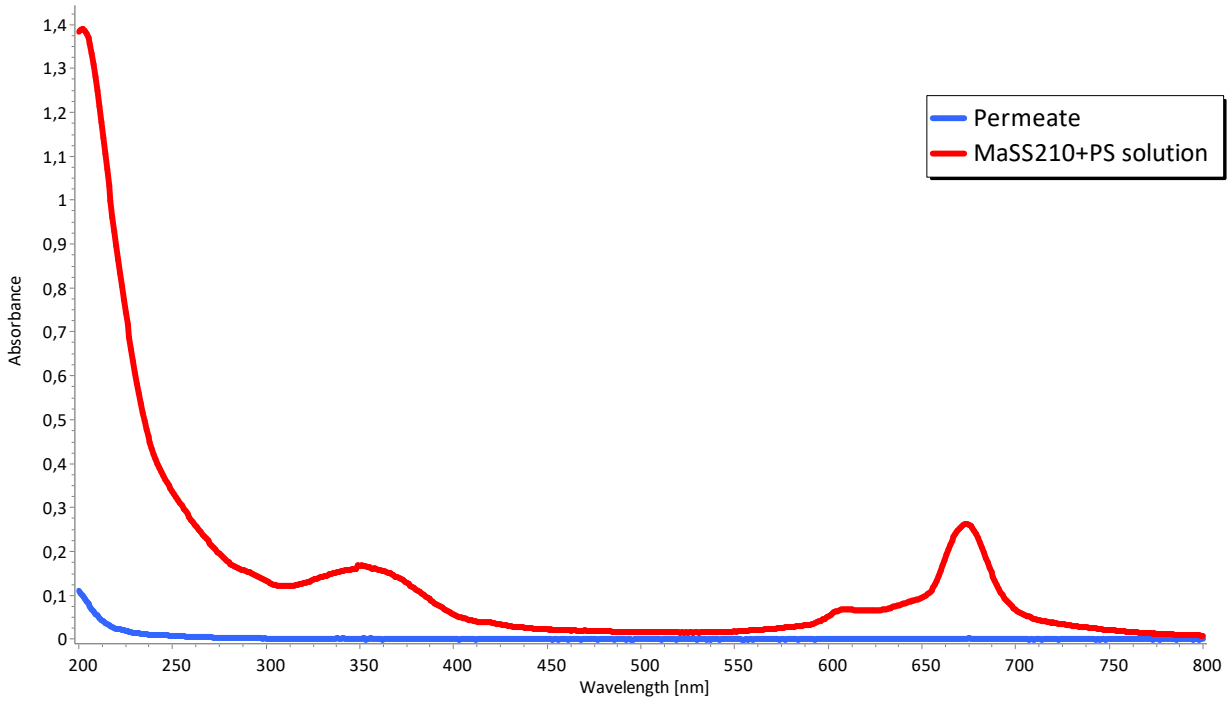

Figure 24: UV-Vis spectra results of the centrifugation filtration test on PS adsorbed on MaSS210 NPs.

The ROS generating ability of the PS/NP system was then tested through a well-established colorimetric method, based on a fluorescein ROS probe (see Figure 23, top). The samples were illuminated for a total of 30 min with a 300W Halogen lamp. It is important to note that the test was for establishing the material properties under irradiation, rather than a biomedical application test. The concentration was chosen based on previously performed tests with charged PMMA NPs loaded with PS. The tests revealed a considerable ROS generation (Figure 25, red curve), similar to that of the AlPCs4 PS in solution (Figure 26, red curve). Intriguingly, the control tests on unloaded NPs revealed similar ROS production activity (Figure 27, yellow and red curves) prompting further investigation into the light-induced properties of the degradable NPs.

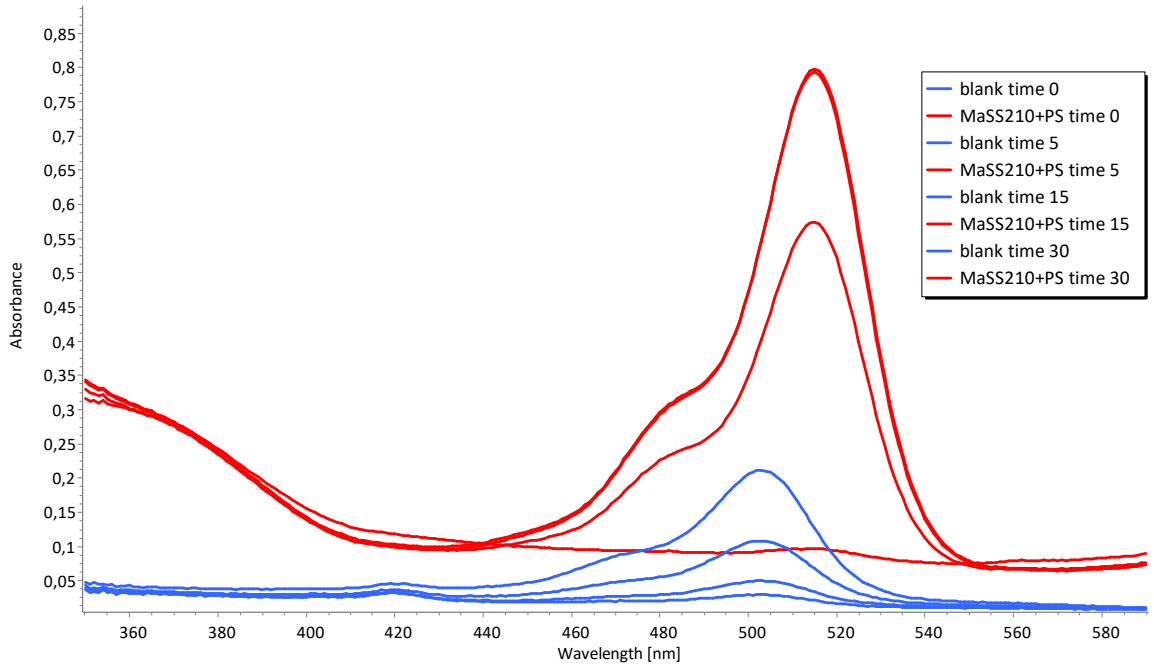

Figure 25: UV-Vis spectra results of the ROS activity studies on MASS210 NPs loaded with AlPCs4 PS (red curves) and a blank solution of ROS probe without NPs as a control sample (blue curves).

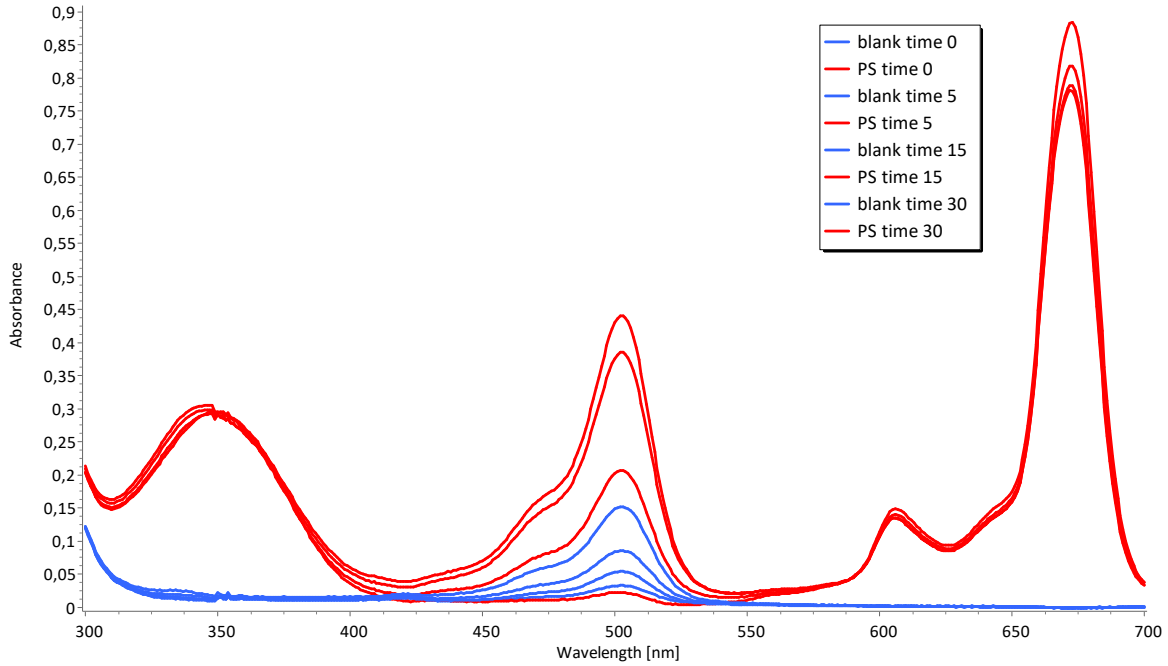

Figure 26: UV-Vis spectra results of the ROS activity studies on AlPCs4 PS in solution (red curves) and a blank solution of ROS probe without PS as a control sample (blue curves). The peak of interest is at 503nm.

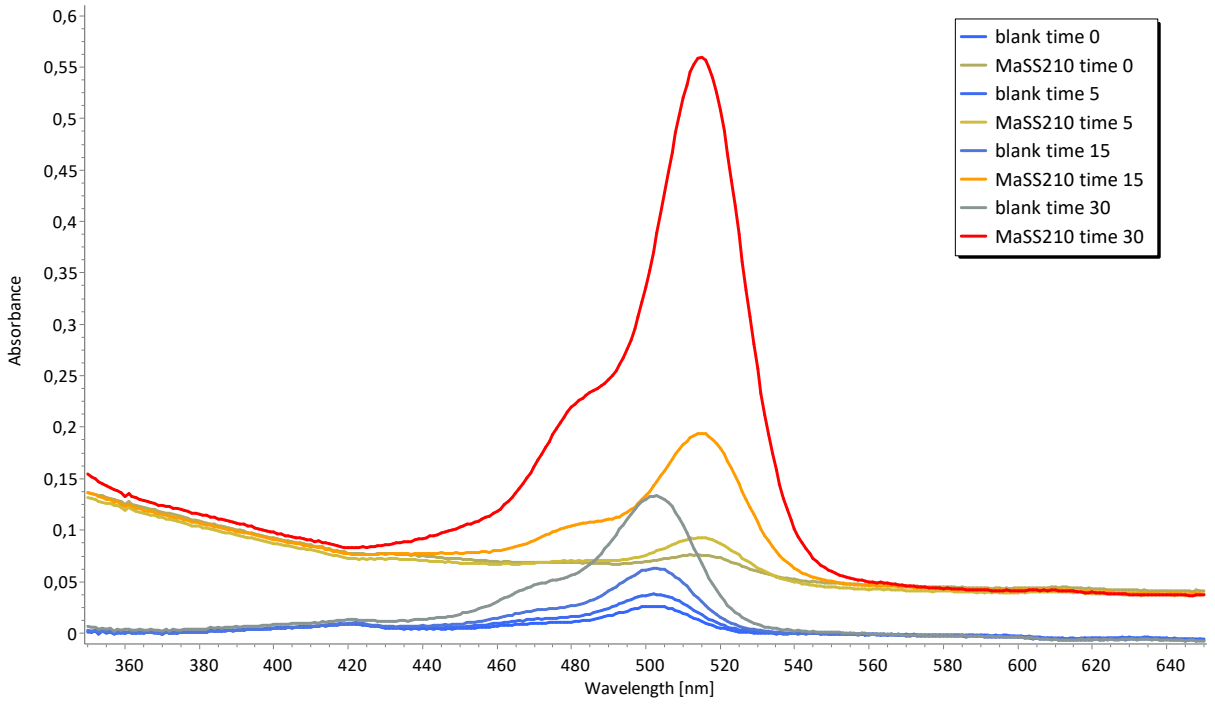

Figure 27: UV-Vis spectra results of the ROS activity studies on unloaded MaSS210 NPs (yellow and red curves) and a blank solution of ROS probe without NPs as a control sample (blue curves).

3.5.1 NPs ROS activity

All previously synthesized NPs were tested via the same approach. The reference non-SS containing PMMA nanoparticles did not show any ROS production (see Figure 28, CTABMA entry). To control for any inconsistencies between test runs and for the semi-quantitative nature of the ROS probe, the change in signal between timestamps was compared, rather than absolute absorbance values. The source of the ROS is believed to be from the S-S bond cleavage upon irradiation, forming thiyl radicals. This is further supported by the lack of ROS activity from the PMMA reference NPs. As the surface TAR functionalization and the PMMA-core are shared between the SS-NPs and the PMMA reference, only the use of the DSDMA (SS-containing) precursor could explain the ROS-producing properties of the SS-NPs. Furthermore, there is clear correlation between the amount of SS in the NPs and intensity of ROS production (see Figure 29). SS450 produces the most ROS of all tested NPs, followed by MASS210 and SS114. MASS100 yields the least amount, only marginally above the non-SS NP and the blank measurement (Figure 28), which is in-line with the previously discussed reasoning of the near-lack of DSDMA within the MASS100 structure.

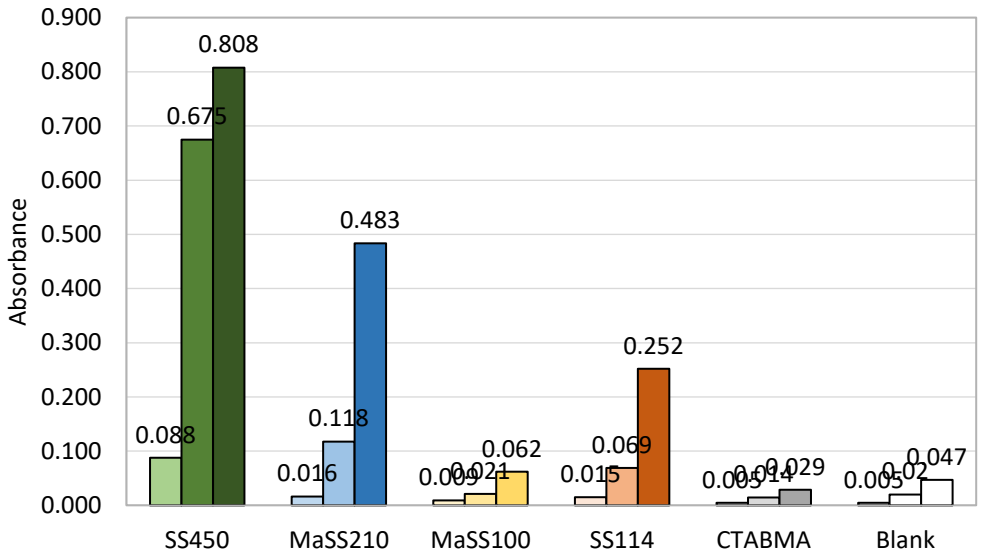

Figure 28: ROS production of the DSDMA-only and MMA-copolymerized NPs. Values represent the maximum absorbance of the 515nm peak, corresponding to the ROS probe at every time interval from 5 mins to 30 mins of total irradiation.

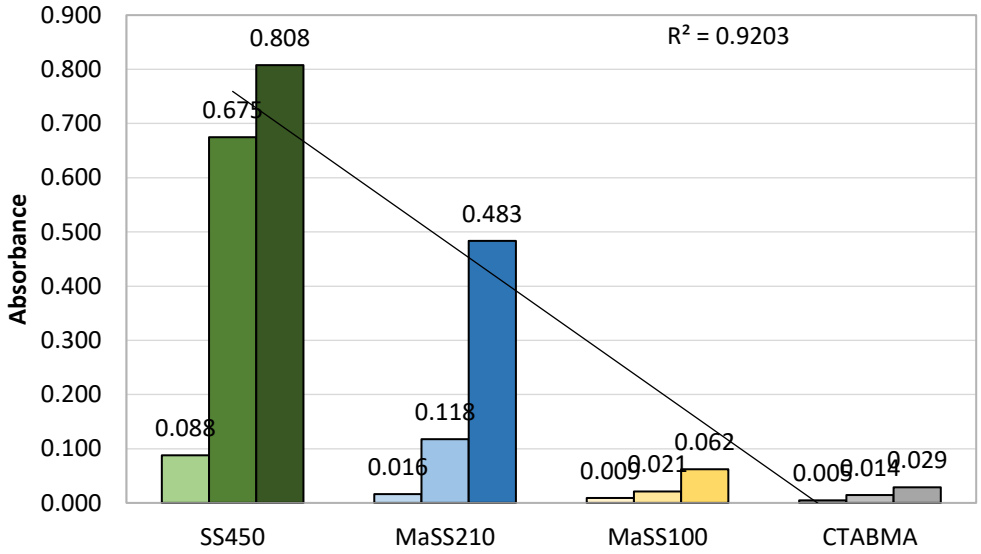

Figure 29: ROS production of the DSDMA-only and MMA-copolymerized NPs. The linear trendline gives the correlation coefficient for the final value of the ROS probe absorbance (~515nm wavelength) indicating a linear correlation between the ROS-production ability of the NPs and their relative disulfide content.

SS114 had similar intended %weight of DSDMA and similar DSDMA peak values to MASS210 and similar overall composition to SS450, however, demonstrated considerably lower ROS activity (see Figure 28, SS114 entry). This phenomenon can only be attributed to the significantly higher amount of TAR within its structure, as no other differences are present between SS450

and SS114. Additionally, the PMMA, present in MASS210, has actually proven to be photo-inert (see CTABMA results) and could not have contributed to ROS activity. The observed behavior could be either due to a direct effect of the TAR residues on the thiyl radical formation and consequent ROS production or due to an indirect effect of larger TAR prevalence on the NP structure/morphology of the polymer chain, affecting the ROS production and detection by the ROS probe. However, any details or the possible mechanism of these potential reactions is not clear. Further mechanistic studies should be performed on the ROS production mechanism to clarify the current results.

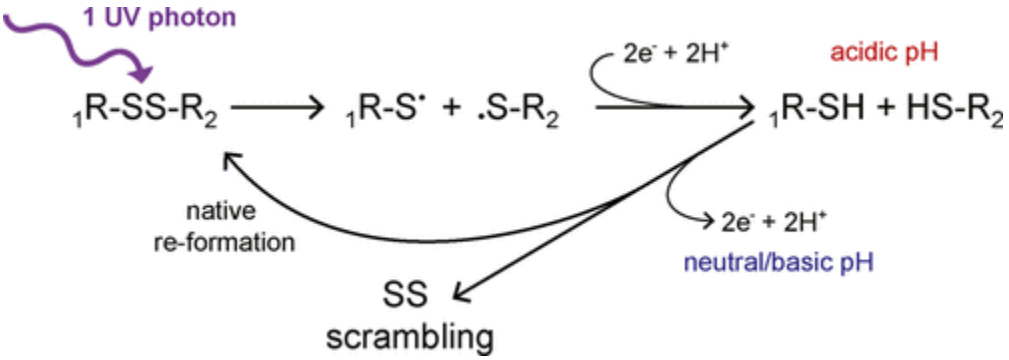

Figure 30: The reaction of UV-induced photocleavage of the disulfide bond yielding thiyl radicals Note: Adapted from https://doi.org/10.1021/acsomega.9b04375

Importantly, as the cutoff for the halogen lamp is not known, the ROS production could be due to the well-studied process of UV-light induced disulfide cleavage into thiyl radicals (see Figure 30), which likely reacted with dissolved oxygen to form ROS (see Figure 31), consequently detected with the probe. The recombination reaction to reform the disulfide bond (figure 31, middle reaction pathway) is unlikely, due to the steric strain of crosslinked system and the limitations of the polymeric structure, relative to the freely dissolved O_2 in solution. Nonetheless, the NPs show considerable ROS production (comparable to that of a known photosensitizer) with a rapid onset. The mechanism of action and the potential triggers should be further investigated. The cleavage of alkyl disulfides to thiyl radicals upon UV-irradiation has been studied and exploited in literature for a variety of catalytic and synthetic applications (Cao & Chen, 2019; Patehebieke, 2020; Wei et al., 2016; Fung et al., 2005). However, to our knowledge, this is the first example of the process for nanoparticle drug carriers, especially under visible light conditions, deserving further investigation potentially not limited to the biomedical field.

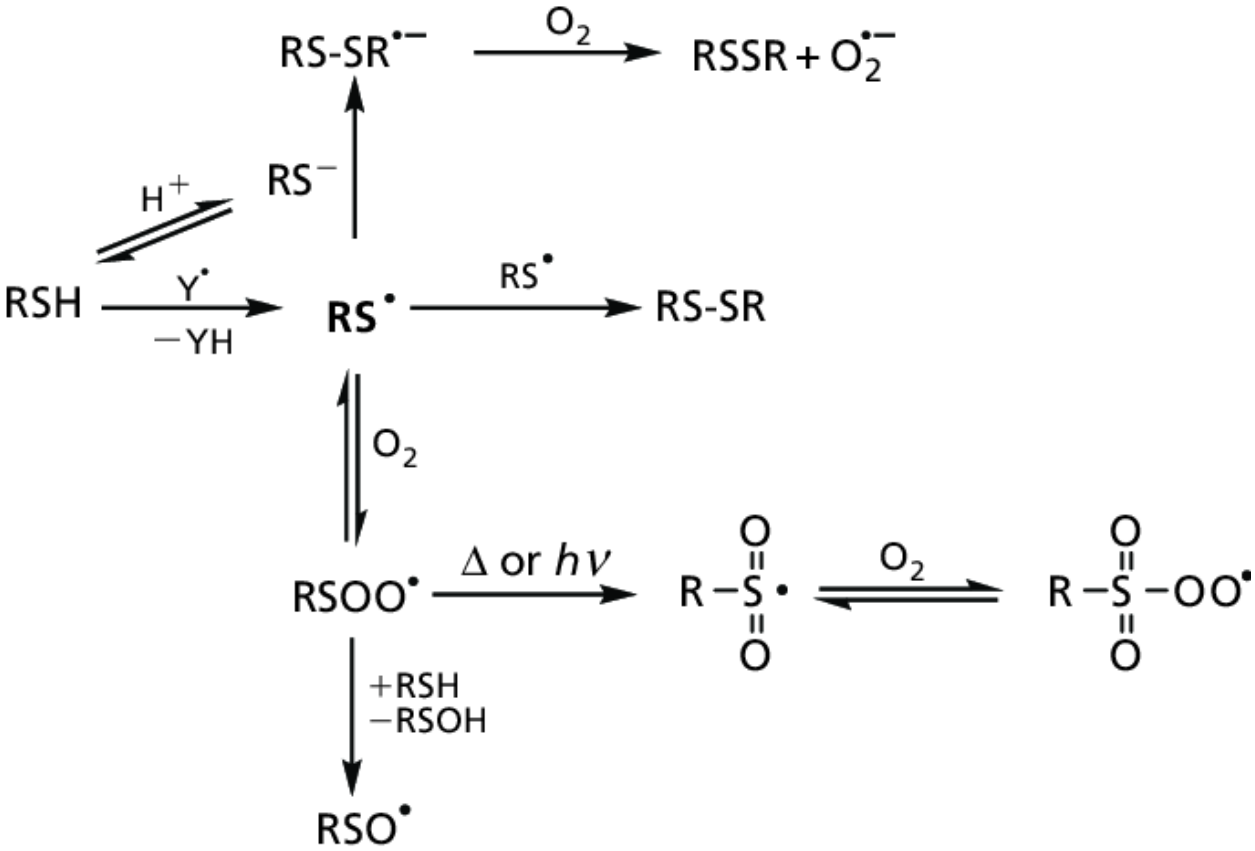

Figure 31: Possible reactions of thiyl radcials, including reactions with molecular oxygen to form ROS (top).
Note: adapted from doi:10.1211/jpp/61.11.0002

3.6 Hydrophobic loading of cargo/Steric encapsulation of cargo

The goal of this experiment was to provide a proof of concept that the developed NPs can encapsulate or be loaded with hydrophobic cargo, while retaining their charged properties and that loading can be achieved during the original TAR-based synthesis process.

After establishing the effectiveness of the synthetic system to produce functional NPs, we attempted to test if the NPs could be loaded with a hydrophobic cargo. Considering that most APIs (especially anticancer agents) are not soluble in aqueous media and sparingly soluble in many common solvents and substances, this ability represents an essential requisite for drug carriers.

The model compound of choice was the Nile Red dye as it is routinely used for loading tests, it can be used for cell culture studies, it is hydrophobic, commercially available and fluorescent, therefore easily detected even in low concentrations (Martinez & Henary, 2016).

The SS114 procedure was used as it proved to produce fully degradable NPs, involved only DSDMA, reducing the variables in the process, and employed a higher TAR/precursor ratio potentially facilitating the encapsulation of the NR in the micelles.

1 mg of Nile Red was introduced to NP synthesis solution in 100 µl of DMSO - a water-miscible solvent, commonly used at low percentages for APIs formulation. In our case, it is expected to be fully removed during the purification steps.

The addition of NR did not induce any notable effects during the synthesis procedure, apart from the obvious color difference from the dye. There was, however, no bulk residue formed, suggesting that the addition of the NR/DMSO solution prevented bulk polymerization. The addition of even the small amount of DMSO (0.1 ml – 1%vol of the reaction solution) could have facilitated solubilization of the large DSDMA droplets, which are considered the source of the bulk polymerization produces. Conversely, it could be the hydrophobic NR that has altered the micellar balance within the solution, facilitating DSDMA encapsulation by TAR and preventing any bulk polymerization. Further, experiments should be performed to test those possibilities.

No changes were observed in the behavior of the solution during the purification. Importantly, NR is hydrophobic, but not completely insoluble in water (0,2 mg/ml). Not-encapsulated NR could potentially be fully removed with the purification procedures; however, it would likely take considerably larger amounts of water than normally used. Furthermore, with the operational amounts (rarely below 10 mL), the NP solution remains sufficient to dissolve the entire amount of NR introduced initially (1 mg). If sufficiently charged, the surface of the NPs should not adsorb NR, however, this is still a possibility. Overall, at this stage, it could not be conclusively proven that all the NR present in the final NP solution is within the NP core.

NR, due to its high hydrophobicity cannot be reliably removed with aqueous methods, however, the use of organic solvents could disrupt the NPs. Either a better purification procedure should be established (e.g., incorporating DMSO as a co-solvent during dialysis), or another drug simulant should be employed, which is more readily removed when not encapsulated by the NPs - e.g., pyrene.

After purification the NR NPs were subjected to the same size and charge tests as the unloaded ones. DLS could not reliably detect size and PDI, most likely due to the NR-induced fluorescence, yet it is unclear whether the NR can disrupt the signal from the core of the NPs or it is positioned on their surface. Nonetheless, the available data indicated that the loaded NPs were of lower diameter and had a slightly lower PDI than their unloaded analogues, while the ζ-potential, albeit a lower value, was strongly positive (see Table 10). Quantification of the amount of loaded NR was not performed.

Table 10: Comparison between the characteristics of the unloaded and loaded analogues.

NP name	Yield	Size (STDev)	PDI (STDev)	ζ-potential
SS114 - unloaded	0,44	113 (9,39)	0,334(0,058)	61,4(3,76)
SS114NR - loaded	0,48	80,6 (29,91)	0,303(0,107)	55,0(1,93)

The TGA analysis also showed considerable similarities between SS114 and on SS114NR, with a higher amount of TAR residues on the surface and slightly lower TAR peak for SS114NR (see Table 11), suggesting less TAR residue within the bulk of the loaded NP. The DSDMA peak was of similar value to that of the unloaded analogue, suggesting that the loaded NPs have a similar redox-sensitivity and degradation potential. As a very low relative amount of NR was loaded on the NPs (>1%wt) any related changes in the decomposition profile of the loaded NPs could not be detected through TGA.

Table 11: Comparison between the TGA data for the two analogues

NP name	DSDMA Weight %	TAR %wt surface	%TAR peak	%DSDMA peak	% MA peak	%Reside TGA
SS114 - unloaded	45,78	12,54	31,32	23,16	31,59	7,040
SS114NR - loaded	46,72	17,41	27,90	20,20	31,44	7,020

Overall, despite the inability to quantify the amount of NR loaded onto the NP, the experiment successfully proved that the DSDMA-based NPs can be successfully synthesized in the presence of a hydrophobic cargo, likely encapsulating it in the process, while retaining their surface charge properties and overall composition.

4 Conclusion and perspectives

Overall, redox-sensitive degradable nanoparticles were successfully synthesized with the DSDMA precursor as a drop-in replacement for MMA. The original emulsion polymerization synthesis pathway was utilized without significant alterations. As expected, the TAR copolymer imparted sufficient surface charge to the NPs, prevented agglomeration and allowed for the electrostatic loading of AlPCs4 photosensitizer, making them suitable for PDT applications. Notably, the novel NPs showed considerable ROS production upon visible light irradiation, even without the addition of any PS. The use of MMA as a copolymer was proven to decrease the NP PDI and slow down degradation, but also reduced ROS production considerably. TGA was demonstrated to be a useful technique for assessing the synthesis efficiency and for analyzing the NP composition. It revealed the preferential polymerization of MMA, rather than DSDMA within the NP structure and the presence of TAR residue not only on the surface, but in the bulk of the synthesized NPs. Finally, introducing a hydrophobic cargo (Nile Red dye) during the synthesis did not disrupt the polymerization process and yielded dye-containing DSDMA-based nanoparticles, which would be the subject of future studies.

The current study has shown the variety of useful properties the novel degradable NP possess, however, has also highlighted several areas that require additional research. Further test should be performed to better understand the polymerization mechanism particularly with a focus on the degree of crosslinking and DSDMA composition of the produced NPs. Ways to more strictly control the NP morphology, especially their PDI, should also be elaborated through further testing and variation of the synthesis procedure.

The accuracy of the TGA analysis should be conclusively evaluated by cross referencing with S-analyzer and N-analyzer readings. To assess the feasibility of the novel degradable NPs for drug applications cytotoxicity tests should be performed both on the NPs and their decomposition products. The encapsulation ability for various APIs should also be evaluated. The synergy between the NP charged surface, hydrophobic core and redox sensitivity should be studied and exploited to potentially provide unique release dynamics for various anticancer agents. Overall, the current research has only set the foundation for an entirely new nanoparticle drug carrier system, which offers numerous opportunities for further research and development and possesses considerable potential to bring future improvements to the field.

5 References

Araujo, L., Sheppard, M., Löbenberg, R., & Kreuter, J. (1999). Uptake of PMMA nanoparticles from the gastrointestinal tract after oral administration to rats: Modification of the body distribution after suspension in surfactant solutions and in oil vehicles. *International Journal of Pharmaceutics*, *176*(2), 209–224. https://doi.org/10.1016/S0378-5173(98)00314-7

Armstrong, B. K., & Kricker, A. (2001). The epidemiology of UV induced skin cancer. *Journal of Photochemistry and Photobiology B: Biology*, *63*(1), 8–18. https://doi.org/10.1016/S1011-1344(01)00198-1

Bettencourt, A., & Almeida, A. J. (2012). Poly(methyl methacrylate) particulate carriers in drug delivery. *Journal of Microencapsulation*, *29*(4), 353–367. https://doi.org/10.3109/02652048.2011.651500

Bizzarri, M., Cucina, A., Conti, F., & D'Anselmi, F. (2008). Beyond the Oncogene Paradigm: Understanding Complexity in Cancerogenesis. *Acta Biotheoretica*, *56*(3), 173–196. https://doi.org/10.1007/s10441-008-9047-8

Boffetta, P., & Nyberg, F. (2003). Contribution of environmental factors to cancer risk. *British Medical Bulletin*, *68*(1), 71–94. https://doi.org/10.1093/bmp/ldg023

Bor, G., Mat Azmi, I. D., & Yaghmur, A. (2019). Nanomedicines for cancer therapy: Current status, challenges and future prospects. *Therapeutic Delivery*, *10*(2), 113–132. https://doi.org/10.4155/tde-2018-0062

Cao, J., & Chen, D.-C. (2019). Disulfide bond photochemistry: The effects of higher excited states and different molecular geometries on disulfide bond cleavage. *Physical Chemistry Chemical Physics*, *21*(8), 4176–4183. https://doi.org/10.1039/C8CP06891G

Cho, H., Bae, J., Garripelli, V. K., Anderson, J. M., Jun, H.-W., & Jo, S. (2012). Redox-sensitive polymeric nanoparticles for drug delivery. *Chemical Communications*, *48*(48), 6043–6045. https://doi.org/10.1039/C2CC31463K

Deda, D. K., & Araki, K. (2015). Nanotechnology, Light and Chemical Action: An Effective Combination to Kill Cancer Cells. *Journal of the Brazilian Chemical Society*, *26*, 2448–2470. https://doi.org/10.5935/0103-5053.20150316

Deng, B., Ma, P., & Xie, Y. (2015). Reduction-sensitive polymeric nanocarriers in cancer therapy: A comprehensive review. *Nanoscale*, *7*(30), 12773–12795. https://doi.org/10.1039/C5NR02878G

Deng, Y., Wei, X.-J., Wang, H., Sun, Y., Noël, T., & Wang, X. (2017). Disulfide-Catalyzed Visible-Light-Mediated Oxidative Cleavage of C=C Bonds and Evidence of an Olefin–Disulfide Charge-Transfer Complex. *Angewandte Chemie International Edition*, *56*(3), 832–836. https://doi.org/10.1002/anie.201607948

Desai, N. (2012). Challenges in Development of Nanoparticle-Based Therapeutics. *The AAPS Journal*, *14*(2), 282–295. https://doi.org/10.1208/s12248-012-9339-4

dos Santos, A. F., de Almeida, D. R. Q., Terra, L. F., Baptista, M. S., & Labriola, L. (2019). Photodynamic therapy in cancer treatment—An update review. *Journal of Cancer Metastasis and Treatment*, *5*. https://doi.org/10.20517/2394-4722.2018.83

Fang, J., Nakamura, H., & Maeda, H. (2011). The EPR effect: Unique features of tumor blood vessels for drug delivery, factors involved, and limitations and augmentation of the effect. *Advanced Drug Delivery Reviews*, *63*(3), 136–151. https://doi.org/10.1016/j.addr.2010.04.009

Ferroni, C., Sotgiu, G., Sagnella, A., Varchi, G., Guerrini, A., Giuri, D., Polo, E., Orlandi, V. T., Marras, E., Gariboldi, M., Monti, E., & Aluigi, A. (2016). Wool Keratin 3D Scaffolds with Light-Triggered Antimicrobial Activity. *Biomacromolecules*, *17*(9), 2882–2890. https://doi.org/10.1021/acs.biomac.6b00697

Fraix, A., Manet, I., Ballestri, M., Guerrini, A., Dambruoso, P., Sotgiu, G., Varchi, G., Camerin, M., Coppellotti, O., & Sortino, S. (2015). Polymer nanoparticles with electrostatically loaded

multicargo for combined cancer phototherapy. *Journal of Materials Chemistry B*, *3*(15), 3001–3010. https://doi.org/10.1039/C5TB00234F

Fung, Y. M. E., Kjeldsen, F., Silivra, O. A., Chan, T. W. D., & Zubarev, R. A. (2005). Facile Disulfide Bond Cleavage in Gaseous Peptide and Protein Cations by Ultraviolet Photodissociation at 157 nm. *Angewandte Chemie International Edition*, *44*(39), 6399–6403. https://doi.org/10.1002/anie.200501533

Gediya, L. K., & Njar, V. C. (2009). Promise and challenges in drug discovery and development of hybrid anticancer drugs. *Expert Opinion on Drug Discovery*, *4*(11), 1099–1111. https://doi.org/10.1517/17460440903341705

Gold nanoparticles immobilized on porous monoliths obtained from disulfide-based dimethacrylate: Application to supported catalysis—ScienceDirect. (n.d.). Retrieved 1 October 2021, from https://www.sciencedirect.com/science/article/pii/S0032386117304020

Greenwell, M., & Rahman, P. K. S. M. (2015). Medicinal Plants: Their Use in Anticancer Treatment. *International Journal of Pharmaceutical Sciences and Research*, *6*(10), 4103–4112. https://doi.org/10.13040/IJPSR.0975-8232.6(10).4103-12

Gudkov, S. V., Shilyagina, N. Yu., Vodeneev, V. A., & Zvyagin, A. V. (2015). Targeted Radionuclide Therapy of Human Tumors. *International Journal of Molecular Sciences*, *17*(1), 33. https://doi.org/10.3390/ijms17010033

Hauner, K., Maisch, P., & Retz, M. (2017). [Side effects of chemotherapy]. *Der Urologe Ausg. A*, *56*(4), 472–479. https://doi.org/10.1007/s00120-017-0338-z

Hofmarcher, T., Lindgren, P., Wilking, N., & Jönsson, B. (2020). The cost of cancer in Europe 2018. *European Journal of Cancer*, *129*, 41–49. https://doi.org/10.1016/j.ejca.2020.01.011

Howard, D. H., Bach, P. B., Berndt, E. R., & Conti, R. M. (2015). Pricing in the Market for Anticancer Drugs. *Journal of Economic Perspectives*, *29*(1), 139–162. https://doi.org/10.1257/jep.29.1.139

Hydrophobic Cysteine Poly(disulfide)-based Redox-Hypersensitive Nanoparticle Platform for Cancer Theranostics—Wu—2015—Angewandte Chemie—Wiley Online Library. (n.d.). Retrieved 1 October 2021, from https://onlinelibrary.wiley.com/doi/abs/10.1002/ange.201503863

Khorsand, B., Lapointe, G., Brett, C., & Oh, J. K. (2013). Intracellular Drug Delivery Nanocarriers of Glutathione-Responsive Degradable Block Copolymers Having Pendant Disulfide Linkages. *Biomacromolecules*, *14*(6), 2103–2111. https://doi.org/10.1021/bm4004805

Kumari, A., Singla, R., Guliani, A., & Yadav, S. K. (2014). Nanoencapsulation for drug delivery. *EXCLI Journal*, *13*, 265–286.

Kumari, A., Yadav, S. K., & Yadav, S. C. (2010). Biodegradable polymeric nanoparticles based drug delivery systems. *Colloids and Surfaces B: Biointerfaces*, *75*(1), 1–18. https://doi.org/10.1016/j.colsurfb.2009.09.001

Laus, M., Sparnacci, K., Lelli, M., Vannini, R., & Tondelli, L. (2000). Core-Shell Functional Nanospheres for Oligonucleoticle Delivery. II. *Journal of Polymer Science, Part A: Polymer Chemistry*, *38*(7), 1110–1117. Scopus. https://doi.org/10.1002/(SICI)1099-0518(20000401)38:7<1110::AID-POLA8>3.0.CO;2-5

Li, Z., Tan, S., Li, S., Shen, Q., & Wang, K. (2017). Cancer drug delivery in the nano era: An overview and perspectives (Review). *Oncology Reports*, *38*(2), 611–624. https://doi.org/10.3892/or.2017.5718

Maeda, H., Wu, J., Sawa, T., Matsumura, Y., & Hori, K. (2000). Tumor vascular permeability and the EPR effect in macromolecular therapeutics: A review. *Journal of Controlled Release*, *65*(1), 271–284. https://doi.org/10.1016/S0168-3659(99)00248-5

Mangal, S., Gao, W., Li, T., & Zhou, Q. (Tony). (2017). Pulmonary delivery of nanoparticle chemotherapy for the treatment of lung cancers: Challenges and opportunities. *Acta Pharmacologica Sinica*, *38*(6), 782–797. https://doi.org/10.1038/aps.2017.34

Martinez, V., & Henary, M. (2016). Nile Red and Nile Blue: Applications and Syntheses of Structural Analogues. *Chemistry – A European Journal*, *22*(39), 13764–13782. https://doi.org/10.1002/chem.201601570

Melancon, M. P., Stafford, R. J., & Li, C. (2012). Challenges to effective cancer nanotheranostics. *Journal of Controlled Release*, *164*(2), 177–182. https://doi.org/10.1016/j.jconrel.2012.07.045

Meyskens, F. L., Jr, Mukhtar, H., Rock, C. L., Cuzick, J., Kensler, T. W., Yang, C. S., Ramsey, S. D., Lippman, S. M., & Alberts, D. S. (2016). Cancer Prevention: Obstacles, Challenges, and the Road Ahead. *JNCI: Journal of the National Cancer Institute*, *108*(2), Article 2. https://doi.org/10.1093/jnci/djv309

Miller, K. D., Nogueira, L., Mariotto, A. B., Rowland, J. H., Yabroff, K. R., Alfano, C. M., Jemal, A., Kramer, J. L., & Siegel, R. L. (2019). Cancer treatment and survivorship statistics, 2019. *CA: A Cancer Journal for Clinicians*, *69*(5), 363–385. https://doi.org/10.3322/caac.21565

Monasterolo, C., Ballestri, M., Sotgiu, G., Guerrini, A., Dambruoso, P., Sparnacci, K., Laus, M., Cesare, M. D., Pistone, A., Beretta, G. L., Zunino, F., Benfenati, V., & Varchi, G. (2012). Sulfonates-PMMA nanoparticles conjugates: A versatile system for multimodal application. *Bioorganic & Medicinal Chemistry*, *20*(22), 6640–6647. https://doi.org/10.1016/j.bmc.2012.09.023

Monsuez, J.-J., Charniot, J.-C., Vignat, N., & Artigou, J.-Y. (2010). Cardiac side-effects of cancer chemotherapy. *International Journal of Cardiology*, *144*(1), 3–15. https://doi.org/10.1016/j.ijcard.2010.03.003

Muhamad, N., Plengsuriyakarn, T., & Na-Bangchang, K. (2018). Application of active targeting nanoparticle delivery system for chemotherapeutic drugs and traditional/herbal medicines in cancer therapy: A systematic review. *International Journal of Nanomedicine*, *13*, 3921–3935. https://doi.org/10.2147/IJN.S165210

Nel, A. E., Mädler, L., Velegol, D., Xia, T., Hoek, E. M. V., Somasundaran, P., Klaessig, F., Castranova, V., & Thompson, M. (2009). Understanding biophysicochemical interactions at the nano-bio interface. *Nature Materials*, *8*(7), 543–557. Scopus. https://doi.org/10.1038/nmat2442

New Insights into "Permeability" as in the Enhanced Permeability and Retention Effect of Cancer Nanotherapeutics. (2017). *ACS Nano*, *11*(10), 9567–9569. https://doi.org/10.1021/acsnano.7b07214

Novio, F. (2020). Design of Targeted Nanostructured Coordination Polymers (NCPs) for Cancer Therapy. *Molecules*, *25*(15), 3449. https://doi.org/10.3390/molecules25153449

Park, W., & Na, K. (2015). Advances in the synthesis and application of nanoparticles for drug delivery. *WIREs Nanomedicine and Nanobiotechnology*, *7*(4), 494–508. https://doi.org/10.1002/wnan.1325

Patehebieke, Y. (2020). An overview on disulfide-catalyzed and -cocatalyzed photoreactions. *Beilstein Journal of Organic Chemistry*, *16*(1), 1418–1435. https://doi.org/10.3762/bjoc.16.118

Pearce, A. K., & O'Reilly, R. K. (2019). Insights into Active Targeting of Nanoparticles in Drug Delivery: Advances in Clinical Studies and Design Considerations for Cancer Nanomedicine. *Bioconjugate Chemistry*, *30*(9), 2300–2311. https://doi.org/10.1021/acs.bioconjchem.9b00456

Perry, M. C. (2008). *The Chemotherapy Source Book*. Lippincott Williams & Wilkins.

Rose, W. C., Clark, J. L., Lee, F. Y. F., & Casazza, A. M. (1997). Preclinical antitumor activity of water-soluble paclitaxel derivatives. *Cancer Chemotherapy and Pharmacology*, *39*(6), 486–492. https://doi.org/10.1007/s002800050603

Rosselgong, J., Armes, S. P., Barton, W., & Price, D. (2009). Synthesis of Highly Branched Methacrylic Copolymers: Observation of Near-Ideal Behavior using RAFT Polymerization. *Macromolecules*, *42*(16), 5919–5924. https://doi.org/10.1021/ma900958a

Rothenberg, M. L., Carbone, D. P., & Johnson, D. H. (2003). Improving the evaluation of new cancer treatments: Challenges and opportunities. *Nature Reviews Cancer*, *3*(4), 303–309. https://doi.org/10.1038/nrc1047

Schober, P., Boer, C., & Schwarte, L. A. (2018). Correlation Coefficients: Appropriate Use and Interpretation. *Anesthesia and Analgesia*, *126*(5), 1763–1768. https://doi.org/10.1213/ANE.0000000000002864

Sharma, A., Houshyar, R., Bhosale, P., Choi, J.-I., Gulati, R., & Lall, C. (2014). Chemotherapy induced liver abnormalities: An imaging perspective. *Clinical and Molecular Hepatology*, *20*, 317–326. https://doi.org/10.3350/cmh.2014.20.3.317

Skeel, R. T., & Khleif, S. N. (2011). *Handbook of Cancer Chemotherapy*. Lippincott Williams & Wilkins.

Sriram, D., Yogeeswari, P., Thirumurugan, R., & Ratan Bal, T. (2005). Camptothecin and its analogues: A review on their chemotherapeutic potential. *Natural Product Research*, *19*(4), 393–412. https://doi.org/10.1080/14786410412331299005

Stein, C. J., & Colditz, G. A. (2004). Modifiable risk factors for cancer. *British Journal of Cancer*, *90*(2), 299–303. https://doi.org/10.1038/sj.bjc.6601509

Sun, H., Cao, D., Liu, Y., Wang, H., Ke, X., & Ci, T. (2018). Low molecular weight heparin-based reduction-sensitive nanoparticles for antitumor and anti-metastasis of orthotopic breast cancer. *Biomaterials Science*, *6*(8), 2172–2188. https://doi.org/10.1039/C8BM00486B

Sun, H., Meng, F., Cheng, R., Deng, C., & Zhong, Z. (2013). Reduction-sensitive degradable micellar nanoparticles as smart and intuitive delivery systems for cancer chemotherapy. *Expert Opinion on Drug Delivery*, *10*(8), 1109–1122. https://doi.org/10.1517/17425247.2013.783009

Sung, H., Ferlay, J., Siegel, R. L., Laversanne, M., Soerjomataram, I., Jemal, A., & Bray, F. (2021). Global Cancer Statistics 2020: GLOBOCAN Estimates of Incidence and Mortality Worldwide for 36 Cancers in 185 Countries. *CA: A Cancer Journal for Clinicians*, *71*(3), 209–249. https://doi.org/10.3322/caac.21660

Swain, S. M. (2011). Chemotherapy: Updates and New Perspectives. *The Oncologist*, *16*(S1), 30–39. https://doi.org/10.1634/theoncologist.2011-S1-30

Szeto, G. L., & Lavik, E. B. (2016). Materials design at the interface of nanoparticles and innate immunity. *Journal of Materials Chemistry B*, *4*(9), 1610–1618. https://doi.org/10.1039/C5TB01825K

Tran, S., DeGiovanni, P.-J., Piel, B., & Rai, P. (2017). Cancer nanomedicine: A review of recent success in drug delivery. *Clinical and Translational Medicine*, *6*(1), 44. https://doi.org/10.1186/s40169-017-0175-0

Tröster, S. D., Müller, U., & Kreuter, J. (1990). Modification of the body distribution of poly(methyl methacrylate) nanoparticles in rats by coating with surfactants. *International Journal of Pharmaceutics*, *61*(1), 85–100. https://doi.org/10.1016/0378-5173(90)90047-8

Tröster, S. D., Wallis, K. H., Müller, R. H., & Kreuter, J. (1992). Correlation of the surface hydrophobicity of 14C-poly(methyl methacrylate) nanoparticles to their body distribution. *Journal of Controlled Release*, *20*(3), 247–260. https://doi.org/10.1016/0168-3659(92)90127-D

Tsai, W.-C., Kung, P.-T., Wang, Y.-H., Kuo, W.-Y., & Li, Y.-H. (2018). Influence of the time interval from diagnosis to treatment on survival for early-stage liver cancer. *PLOS ONE*, *13*(6), e0199532. https://doi.org/10.1371/journal.pone.0199532

Varchi, G., Benfenati, V., Pistone, A., Ballestri, M., Sotgiu, G., Guerrini, A., Dambruoso, P., Liscio, A., & Ventura, B. (2013). Core—Shell poly-methylmethacrylate nanoparticles as effective carriers of electrostatically loaded anionic porphyrin. *Photochemical & Photobiological Sciences*, *12*(5), 760–769. https://doi.org/10.1039/c2pp25393c

Wang, K., Peng, H., Thurecht, K. J., Puttick, S., & Whittaker, A. K. (2014). Biodegradable core crosslinked star polymer nanoparticles as 19F MRI contrast agents for selective imaging. *Polymer Chemistry*, *5*(5), 1760–1771. https://doi.org/10.1039/C3PY01311A

Wang, L., Huo, M., Chen, Y., & Shi, J. (2018). Tumor Microenvironment-Enabled Nanotherapy. *Advanced Healthcare Materials*, *7*(8), 1701156. https://doi.org/10.1002/adhm.201701156

Warneke, J., Wang, Z., Zeller, M., Leibfritz, D., Plaumann, M., & Azov, V. A. (2014). Methacryloyl chloride dimers: From structure elucidation to a manifold of chemical transformations. *Tetrahedron*, *70*(37), 6515–6521. https://doi.org/10.1016/j.tet.2014.07.019

Wu, S., Zhu, W., Thompson, P., & Hannun, Y. A. (2018). Evaluating intrinsic and non-intrinsic cancer risk factors. *Nature Communications*, *9*(1), 3490. https://doi.org/10.1038/s41467-018-05467-z

Xu, Z., Wang, D., Xu, S., Liu, X., Zhang, X., & Zhang, H. (2014). Preparation of a Camptothecin Prodrug with Glutathione-Responsive Disulfide Linker for Anticancer Drug Delivery. *Chemistry – An Asian Journal*, *9*(1), 199–205. https://doi.org/10.1002/asia.201301030

Zugazagoitia, J., Guedes, C., Ponce, S., Ferrer, I., Molina-Pinelo, S., & Paz-Ares, L. (2016). Current Challenges in Cancer Treatment. *Clinical Therapeutics*, *38*(7), 1551–1566. https://doi.org/10.1016/j.clinthera.2016.03.026

6 Appendix

6.1 NMR spectra

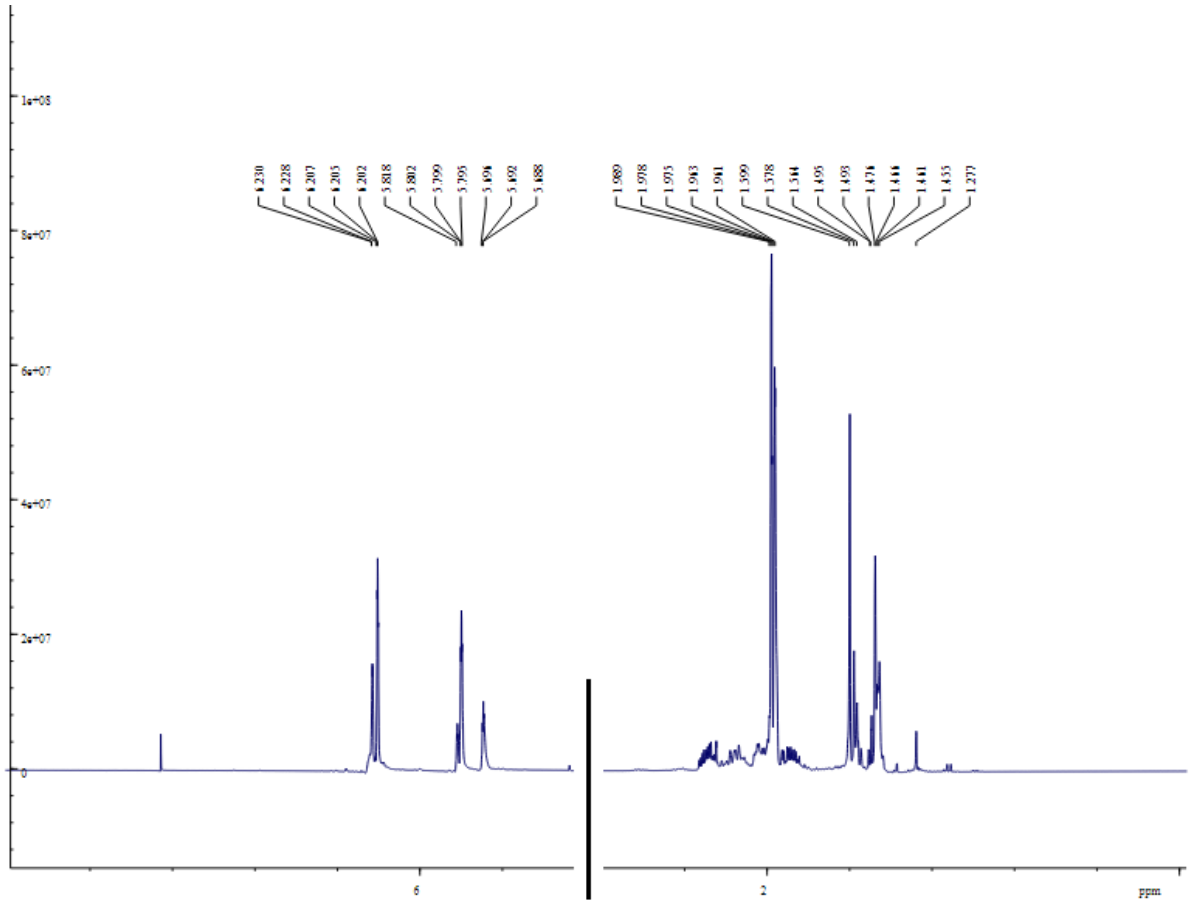

Figure A: NMR Spectrum of MAAnh used for the synthesis of DSDMA (impurities evident at <2ppm).

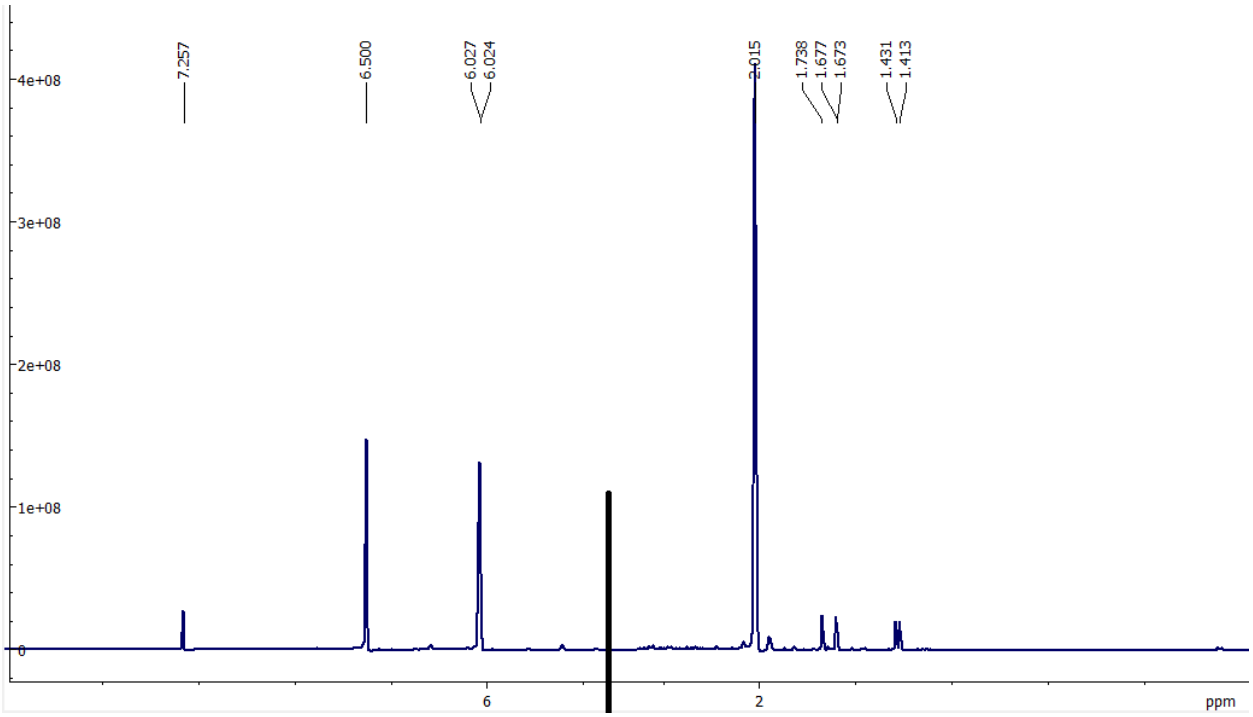

Figure B: NMR Spectrum of the distilled MAACl used for the synthesis of DSDMA (low levels of impurities evident at <2ppm).

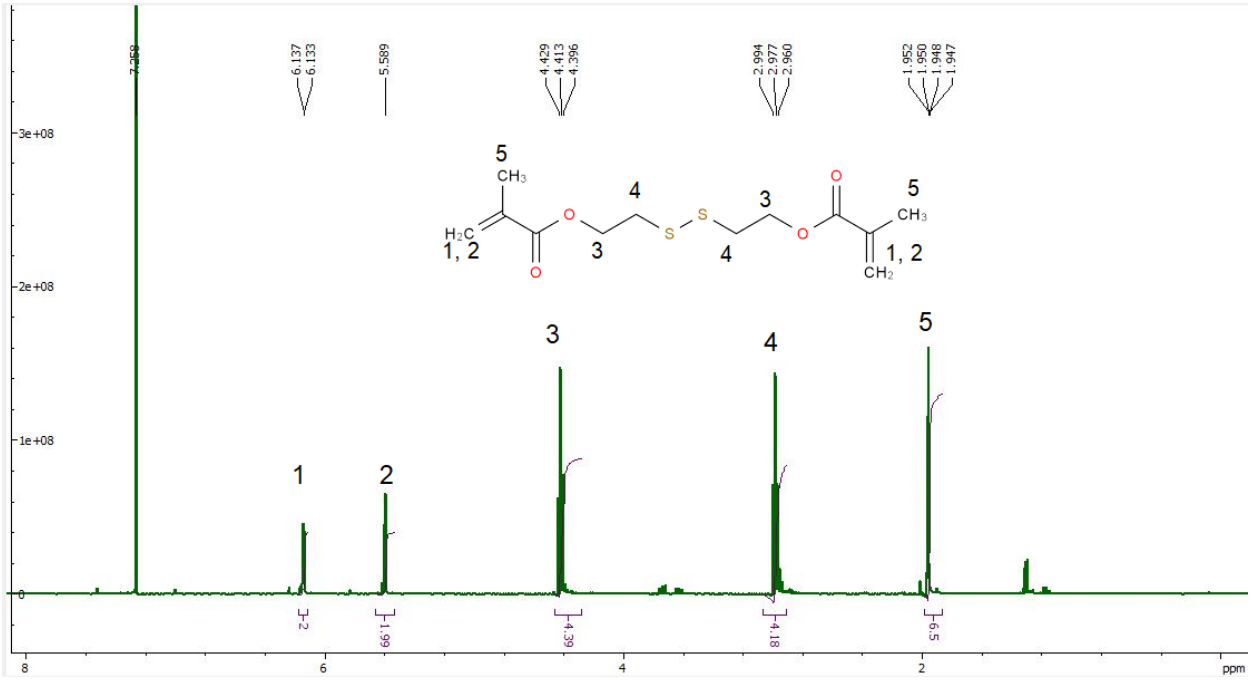

Figure C: NMR Spectrum of DSDMA used for the NP synthesis

6.2 Full UV-Vis spectra

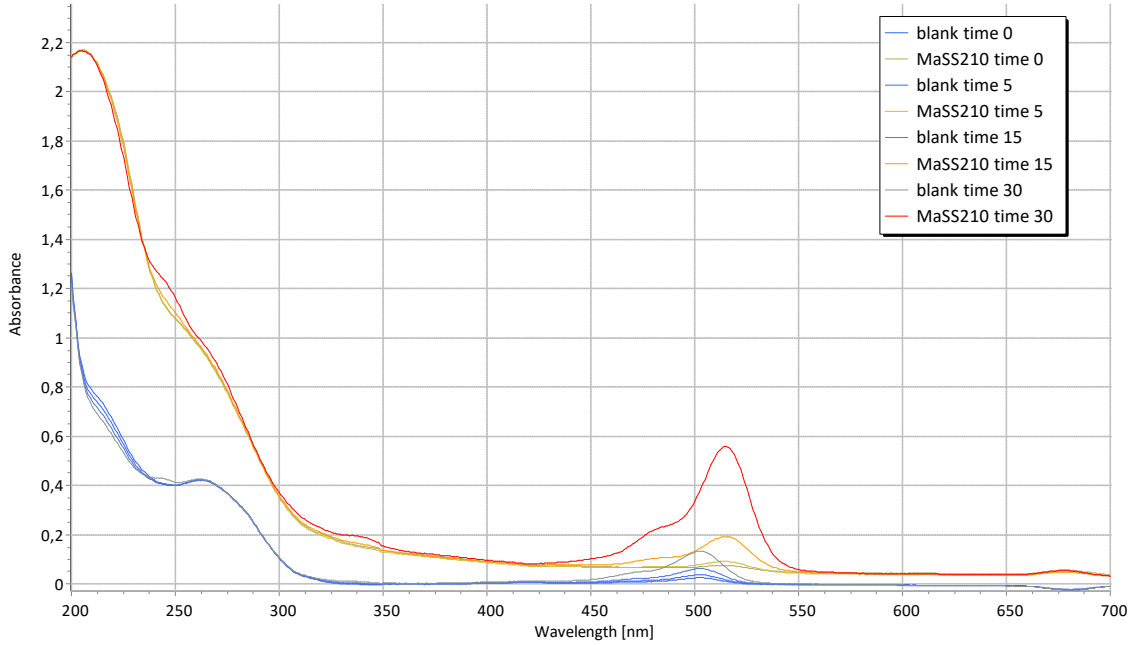

Figure D: Full UV-Vis spectrum of the unloaded MaSS210 NPs (yellow, red) vs blank (blue)

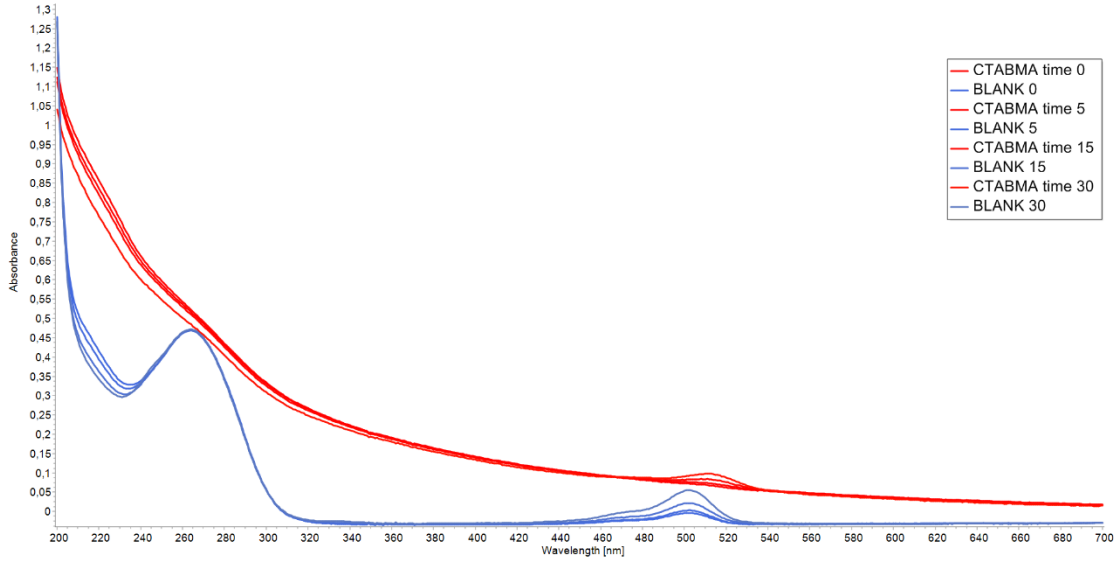

Figure E: Full UV-Vis spectrum of the CTABMA NPs (red) vs blank (blue)

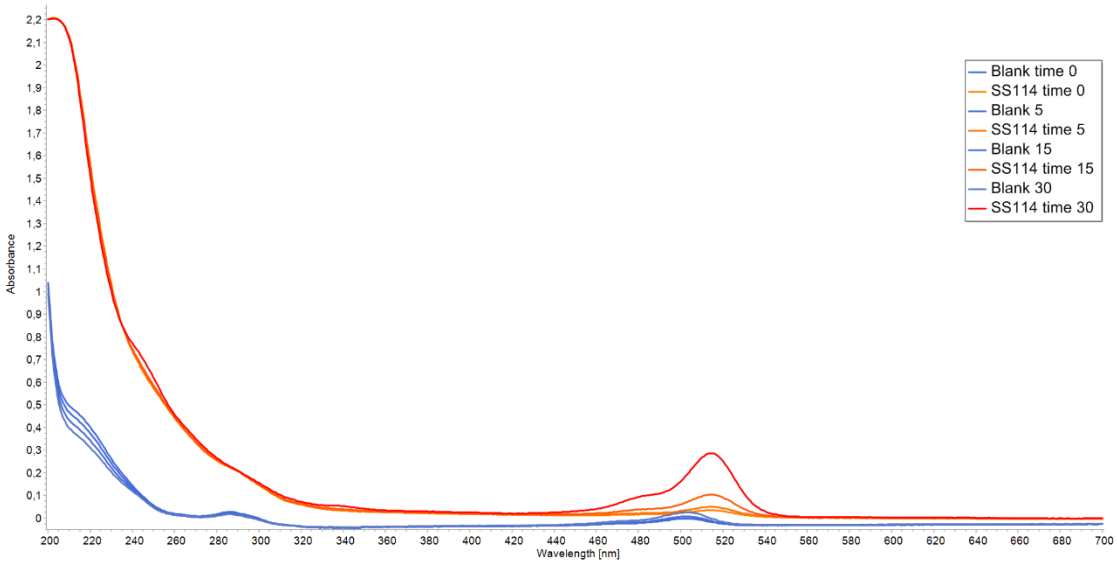

Figure F: Full UV-Vis spectrum of the SS114 NPs (red) vs blank (blue)

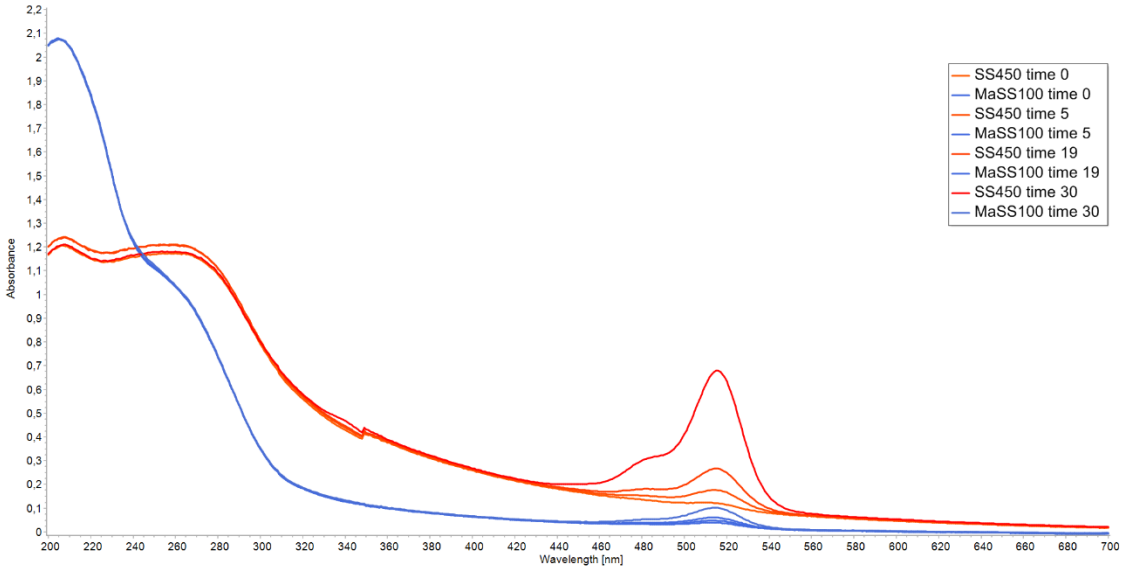

Figure G: Full UV-Vis spectrum of the SS450 NPs (red) vs the MaSS100 NPs (blue)

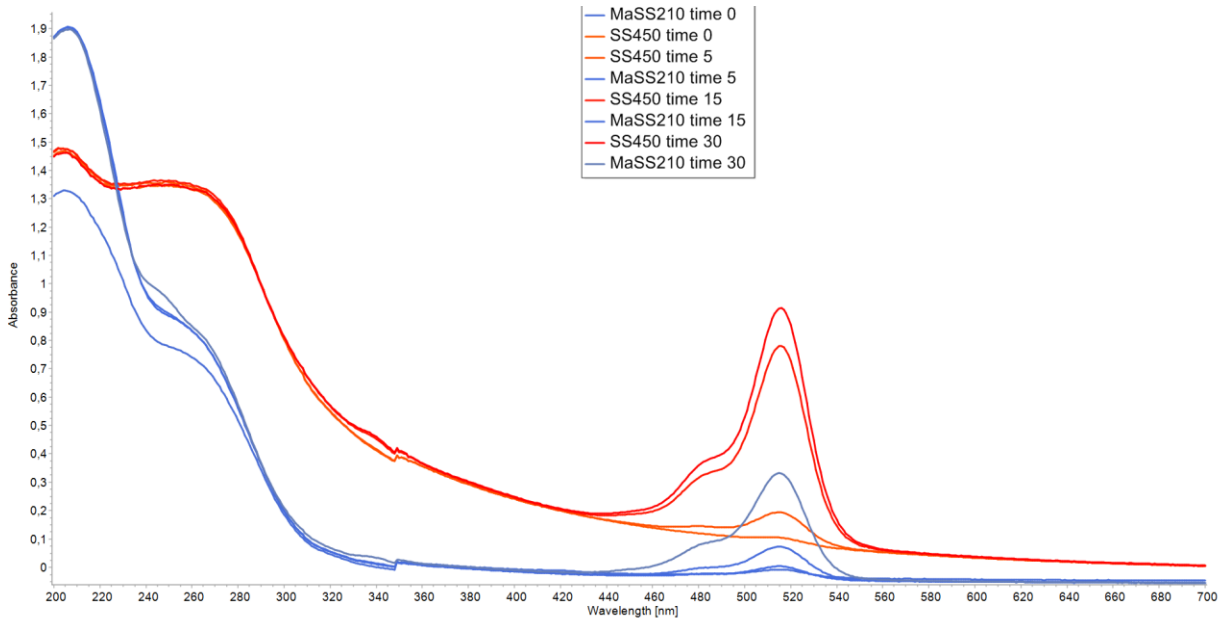

Figure H: Full UV-Vis spectrum of the SS450 NPs (red) vs the MaSS210 NPs (blue)